IL-1β+ macrophages fuel pathogenic inflammation in pancreatic cancer

IL-1β$^+$ macrophages fuel pathogenic inflammation in pancreatic cancer

Nicoletta Caronni[1,§,*], Federica La Terza[1,§], Francesco M. Vittoria[1,2,§], Giulia Barbiera[1,§], Luca Mezzanzanica[1,2], Vincenzo Cuzzola[1,2], Simona Barresi[1], Marta Pellegatta[3], Paolo Canevazzi[3], Garett Dunsmore[4], Carlo Leonardi[1], Elisa Montaldo[1], Eleonora Lusito[1], Erica Dugnani[5], Antonio Citro[5], Melissa S.F. Ng[6], Marco Schiavo Lena[3], Denise Drago[7], Annapaola Andolfo[7], Silvia Brugiapaglia[8], Alessandro Scagliotti[8], Alessandra Mortellaro[1], Vincenzo Corbo[9], Zhaoyuan Liu[10], Anna Mondino[3], Paolo Dellabona[3], Lorenzo Piemonti[2,5], Carla Taveggia[3], Claudio Doglioni[2,3], Paola Cappello[8], Francesco Novelli[8], Matteo Iannacone[2,3], Lai Guan Ng[6], Florent Ginhoux[4,6,10], Stefano Crippa[2,11], Massimo Falconi[2,11], Chiara Bonini[2,3], Luigi Naldini[1,2], Marco Genua[1], and Renato Ostuni[1,2,*].

[1]San Raffaele Telethon Institute for Gene Therapy (SR-Tiget), IRCCS San Raffaele Scientific Institute, Milan, Italy. [2]Vita-Salute San Raffaele University, Milan, Italy. [3]IRCCS San Raffaele Scientific Institute, Milan, Italy. [4]INSERM U1015, Gustave Roussy Cancer Campus, Villejuif, 94800, France. [5]Diabetes Research Institute (DRI), IRCCS San Raffaele Scientific Institute, Milan, Italy. [6]Singapore Immunology Network (SIgN), A*STAR, Biopolis, Singapore. [7]Center for Omics Sciences (COSR), IRCCS San Raffaele Scientific Institute, Milan, Italy. [8]Department of Molecular Biotechnology and Health Sciences, University of Turin, Turin, Italy. [9]University of Verona, Verona, Italy. [10]Shanghai Institute of Immunology, Department of Immunology and Microbiology, Shanghai Jiao Tong University School of Medicine, Shanghai 200025, China. [11]Pancreas Translational and Clinical Research Center, IRCCS San Raffaele Scientific Institute, Milan, Italy. [§] equal contribution [*] corresponding authors (caronni.nicoletta@hsr.it, ostuni.renato@hsr.it)

Pancreatic ductal adenocarcinoma (PDAC) is a lethal disease with high resistance to therapies[1]. Inflammatory and immunomodulatory signals co-exist in the pancreatic tumor microenvironment (TME), leading to dysregulated reparative and cytotoxic responses. Tumor-associated macrophages (TAMs) are key players in the TME[2], but their diversity hampered full therapeutic exploitation of these cells. Here, we combined single-cell and spatial genomics with functional experiments to elucidate macrophage functions in PDAC. We uncovered an inflammatory loop between tumor cells and interleukin (IL)-1β$^+$ TAMs, a subset of macrophages elicited by a local synergy between prostaglandin E_2 (PGE_2) and tumor necrosis factor (TNF)-α. Physical proximity with IL-1β$^+$ TAMs was associated with inflammatory reprogramming and acquisition of enhanced pathogenic properties by a subset of PDAC cells. Interfering with the PGE_2-IL-1β axis elicited TAM reprogramming and antagonized tumor cell-intrinsic and -extrinsic inflammation, leading to PDAC control *in vivo*. IL-1β$^+$ TAMs are conserved across human cancers and correlate with tumor-intrinsic inflammation. Targeting IL-1β$^+$ TAMs may represent a preventive or therapeutic strategy to reprogram immune dynamics in cancer.

Macrophages play key roles in tissue homeostasis, immunity and repair[3]. The functional diversity of these cells is enabled by plastic adaptations to environmental cues via the selection of genomic programs by lineage-determining and stimulus-responsive transcription factors[4,5]. Tumor-associated macrophages (TAMs) are relevant targets in immune oncology, as their abundance generally correlates with resistance to therapy, metastasis and poor patient survival[6]. However, single-cell RNA sequencing (scRNA-Seq) studies have shown that TAMs are highly heterogenous and include subsets with diverse ontogenies, functions, and therapeutic potential[7]. Furthermore, macrophage activities are locally influenced by cellular, physical and chemical interactions within tissue niches[8].

In tumors, protective immunity triggered by sensing of cell death and danger-associated molecular patterns (DAMPs) co-exists with programs that suppress cytotoxic responses and that stimulate tissue repair[9,10]. Exposure to these complex mixtures of signals in the tumor microenvironment (TME) underlies recurrent findings that, rather than mirroring *in vitro* activation states, TAMs co-express genes encoding for immune stimulatory, immune modulatory and reparative factors[11-13]. In this view, TAM behaviors recapitulate physiological programs of macrophages that are co-opted to promote disease[14].

The pancreatic TME is enriched in factors that hamper the recruitment and/or activation of dendritic cells (DC), cytotoxic natural killer (NK) cells and T lymphocytes[15]. On the other hand, PDAC is infiltrated by TAMs and other myeloid cells that trigger inflammation, fuel angiogenesis and promote aberrant matrix deposition[1]. Inflammatory programs can functionally cooperate with oncogenic mutations to increase the risk of cancer development[16]. For instance, inflammatory responses to pancreatic injury trigger persistent epigenetic changes in epithelial cells that underlie non-resolving metaplasia and accelerated tumorigenesis upon subsequent *Kras* activation[17,18]. In this study, we set out to elucidate the cellular and molecular determinants of pathogenic inflammation in pancreatic cancer.

IL-1β$^+$ TAMs correlate with poor prognosis in human PDAC.

We performed scRNA-Seq of freshly dissociated tumor samples from naïve or chemotherapy-treated PDAC patients (**Supplementary Table 1**). The ensuing dataset contained 59,569 single-cell transcriptomes spanning the tumor, epithelial, stromal, and immune compartments across patients and treatment conditions (**Fig. 1a, Extended Data Fig. 1a-b, Supplementary Table 1**). Sub-clustering of mononuclear phagocytes (MNPs) uncovered distinct subsets of TAMs, whose relative abundance and gene expression programs were largely conserved between naïve and chemotherapy-treated patients (**Fig. 1a-b, Extended Data Fig. 1c-h**). *SPP1*$^+$ TAMs expressed lipid metabolism (*FBP1*, *APOC1*) and phagocytic receptor (*MARCO*, *MERTK*) genes, corresponding to populations described in liver, colorectal and non-small cell lung cancer[19-22]; *FOLR2*$^+$ TAMs expressed non-canonical myeloid markers (*LYVE1, SELENOP*) and matched *bona fide* resident macrophages in normal tissues[23-25] and human tumors[20,26]; other clusters of TAMs expressed metallothionein (*MT1G*, *MT1X*, *MT1E*), heat-shock protein (*HSP*), or cell cycle (*TOP2A*, *MKI67*) genes (**Fig. 1a-b, Extended Data Fig. 1i, Supplementary Table 1**). Our analysis uncovered *IL1B*$^+$ TAMs, a subset of PDAC macrophages whose transcriptome was enriched in inflammatory response (*IL1B, TNF, NLRP3, PTGS2*), leukocyte recruitment (*CXCL1, CXCL2, CCL3*) and angiogenesis (*VEGFA, THBS1, PDGFB*) programs but was depleted of interferon (IFN) response and antigen presentation gene ontology (GO) terms (**Fig. 1b-d, Supplementary Table 1**). We next computed gene signatures for each TAM subset by selecting marker genes in scRNA-Seq data and filtering out non MNP-specific transcripts. Expression of the *IL1B*$^+$ TAM signature in RNA-Seq data from The Cancer Genome Atlas (TCGA) was associated with poor patient survival, but not with overall macrophage abundance (**Fig. 1e, Extended Data Fig. 1j**, **Supplementary Table 1**). Re-analysis of bulk[27] and scRNA-Seq data showed up-regulation of the *IL1B*$^+$ TAM gene signature in blood monocytes from PDAC patients, although expression

levels of the module remained lower than in tumor-infiltrating cells (**Extended Data Fig. 1k-l**). These data uncover *IL1B*$^{+}$ TAMs as a subset of PDAC macrophages characterized by inflammatory and non-cytotoxic transcriptional programs, whose predicted abundance correlated with poor patient prognosis.

IL-1β^{+} TAMs are conserved in mouse models of pancreatic cancer.

We next profiled a mouse model of pancreatic cancer whereby *Kras*$^{G12D/+}$ *Trp53*$^{R172H/+}$ *Pdx1*$^{Cre/+}$ (KPC) cells[28] are injected orthotopically in immune-competent recipients. Cells from blood, pancreas and tumors at day 10, 20 and 30 post inoculation were subjected to scRNA-Seq, followed by iterative clustering and annotation of 6,996 macrophage transcriptomes (**Fig. 2a-b, Extended Data Fig. 2a-c, Supplementary Table 2**). Key marker genes and transcriptional programs of *Il1b*$^{+}$ TAMs, as well as of *Folr2*$^{+}$, *Spp1*$^{+}$, and proliferating TAMs, were conserved between mice and men (**Fig. 2c, Extended Data Fig. 2d, Supplementary Table 2**). These subsets were consistently identified by scRNA-Seq in orthotopic or subcutaneous *Kras*$^{G12D/WT}$ *Pdx1*$^{Cre/WT}$ (KC) models, or in autochthonous tumors from KPC mice (**Extended Data Fig. 2e, Supplementary Table 2**). Having observed an early and persistent accumulation of *Il1b*$^{+}$ TAMs in mouse PDAC (**Fig. 2d**), we set out to characterize the phenotype of these cells. In keeping with scRNA-Seq analyses, IL-1β was undetectable in pancreatic macrophages from control mice whereas a substantial fraction of TAMs expressed IL-1β in PDAC (**Fig. 2e**). IL-1β^{+} TAMs were characterized by high expression of CD64, CD11c, major histocompatibility complex II (MHC II) and costimulatory molecules CD80 and CD86, together with known markers of immune dysfunction in cancer such as CD206, arginase 1 (ARG1) and the immune checkpoint inhibitor PD-L1 (**Fig. 2f, Extended Data Fig. 2f**). These data establish IL-1β^{+} TAMs as a conserved macrophage population co-expressing inflammatory and immune inhibitory markers.

Monocytes differentiate into IL-1β$^+$ TAMs upon exposure to TME factors.

Time-resolved scRNA-Seq datasets of mouse monocytes and macrophages from blood, pancreas, or tumors were integrated and subjected to optimal-transport (OT) analysis to infer ancestor-descendant relationships[29]. We found that IL-1β$^+$ TAMs had higher probability to derive from monocytes than *bona fide* resident *Clps*$^+$ or *Folr2*$^+$ macrophages (**Fig. 3a, Extended Data Fig. 3a-i**). CellRank analyses[30] also uncovered a trajectory linking tumor-infiltrating monocytes and IL-1β$^+$ TAMs (**Fig. 3b-c, Extended Data Fig. 3j**), with key marker genes of IL-1β$^+$ TAMs – *Il1b*, *Ptgs2* and *Cxcl2*, among others – driving the predicted transition (**Fig. 3d, Supplementary Table 3**). These transcripts were up-regulated as monocytes entered the tumor and progressively acquired IL-1β$^+$ TAM identity in mouse and human PDAC (**Fig. 3e-f, h-i**). Accordingly, protein levels of IL-1β were low in circulating monocytes from control and tumor-bearing mice but increased substantially upon recruitment to tumors (**Fig. 3g**). We next performed lineage tracing with *Ms4a3*^{CreERT2}-*Rosa*^{TdT} mice, in which tamoxifen elicits irreversible expression of a fluorescent reporter in granulocyte-monocyte precursors (GMP) and their progeny[31]. These experiments showed that the vast majority of IL-1β$^+$ TAMs from pancreatic tumors was tdTomato$^+$ (**Fig. 3j**). Thus, IL-1β$^+$ TAMs originate from circulating monocytes that infiltrate the tumor and become exposed to local factors in the TME.

PGE_2 and TNF-α cooperatively elicit the IL-1β$^+$ TAM state.

We observed an enrichment of IL-1 and TNF response GO terms within driver genes of the monocyte-to-IL-1β$^+$ TAM transition (**Extended Data Fig. 4a, Supplementary Table 3**). The transcriptome of IL-1β$^+$ TAMs was enriched in genes induced by IL-1β or TNF-α in mouse macrophages[32], and both molecules were detectable in human PDAC (**Extended Data Fig. 4b-c, Supplementary Table 4**). However, treatment of mouse bone marrow-derived macrophages (BMDMs) with IL-1β or TNF-α did not elicit IL-1β synthesis, highlighting a requirement for

additional factors (**Extended Data Fig. 4d**). Previous studies found that the eicosanoid prostaglandin E_2 (PGE_2), a known regulator of the immune TME[33], can stimulate IL-1β production while suppressing IFN responses in macrophages[34-36]. We detected high levels of PGE_2 in biopsies of human and mouse PDAC or in culture supernatant of KPC and KC cells, and PGE_2-induced genes[35] were over-represented in IL-1β$^+$ TAMs (**Fig. 4a-b, Extended Data Fig. 4e-g, Supplementary Table 4**). We thus tested whether PGE_2 contributed to elicit the IL-1β$^+$ TAM state. PGE_2 alone had limited effects, but its co-administration with TNF-α – not with IL-1β – triggered potent IL-1β synthesis in BMDMs and monocytes (**Fig. 4c-h**, **Extended Data Fig. 4h-i**). RNA-Seq analyses in BMDMs identified dozens of transcripts synergistically induced by PGE_2+TNF-α, which were over-represented in IL-1β$^+$ TAMs and within the driver genes of monocyte-to-IL-1β$^+$ TAM transition (**Fig. 4i**, **Extended Data Fig. 4j-k, Supplementary Table 4**); these genes encoded for factors that elicit tumor-promoting inflammation (*Il1b*, *Il6*) while suppressing cytotoxic immunity (*Il10*), or that stimulate prostaglandin synthesis (*Ptges, Ptgs2*), myeloid cell recruitment (*Cxcl1, Cxcl2, Cxcl3*), and tissue repair (*Areg, Arg2, Wnt11, Il33*) (**Extended Data Fig. 4j, l, Supplementary Table 4**). Multiplexed analyses of proteins in the supernatant confirmed elevated synthesis of IL-6 and IL-10 by co-stimulated macrophages, while revealing PGE_2-driven suppression of CCL5, CXCL10, CXCL11, and CXCL16 – chemokines with key roles in cytotoxic T and NK cell recruitment (**Extended Data Fig. 4m**). These data identify PGE_2 and TNF-α as TME factors able to cooperatively elicit the IL-1β$^+$ TAM state in PDAC.

IL-1β$^+$ TAMs accumulate in areas of inflammation, hypoxia and angiogenesis.

Immunofluorescence (IF) analyses of orthotopic mouse PDAC highlighted a preferential distribution of IL-1β$^+$ TAMs in fibroblast-rich stromal regions surrounding the tumor core, with differential distribution of TAM subsets being detectable already at early time points as

well as in human PDAC (**Fig. 5a-c, Extended Data Fig. 5a**). We next performed paired single-cell and spatial transcriptome (ST) analyses of mouse PDAC. Transcript-based deconvolution of cell subsets was concordant with protein expression (**Fig. 5d-e, Extended Data Fig. 5b-e, Supplementary Table 5**). Spatial Principal Components (sPC) analyses discriminated ST spots enriched in IL-1β$^+$, FOLR2$^+$, or SPP1$^+$ TAMs (**Fig. 5f, Extended Data Fig. 5f-i, Supplementary Table 5**). Projection of PGE_2+TNF-α synergized gene signature onto ST data uncovered a broad overlap with spots enriched in IL-1β$^+$ TAMs (**Fig. 5g, Extended Data Fig. 5j**). More generally, IL-1β$^+$ TAM regions were enriched in inflammation, hypoxia, angiogenesis, and wound healing GO terms (**Fig. 5h, Extended Data Fig. 5k-l, Supplementary Table 5**). These predictions were validated by IF analyses showing proximity of IL-1β$^+$ TAMs to CD31$^+$VEGFR2$^+$ endothelial cells and hypoxic areas (**Fig. 5i-l**). We conclude that IL-1β$^+$ TAMs undergo local specification in inflamed, angiogenic and hypoxic regions of PDAC associated to high PGE_2 and TNF-α synergistic activity.

PDAC-derived PGE_2 elicits IL-1β$^+$ TAMs and promotes tumor growth.

To assess the role of PGE_2 in PDAC, we treated immune competent mice with celecoxib, a selective inhibitor of the prostaglandin biosynthetic enzyme cyclo-oxygenase (COX)-2, concomitant with tumor challenge. This treatment lowered PGE_2 levels in tumors, and it was associated with reduced accumulation of IL-1β$^+$ TAMs and monocytes, increased infiltration of cytotoxic GZMB$^+$ CD8$^+$ T cells, and delayed tumor growth (**Extended Data Fig. 6a-d**). Because cancer cells produce high levels of PGE_2 (**Extended Data Fig. 4f**), we generated COX-2 ko PDAC cell lines that were unable to produce the latter eicosanoid but did not show defects in viability or proliferation *in vitro* (**Fig. 6a, Extended Data Fig. 6e-g, Supplementary Table 6**). COX-2 ko PDAC cells or spheroids efficiently engrafted in immune competent mice but their growth was controlled in a CD8$^+$ T cell- and NK cell-dependent manner, in keeping

with an observed increase of lymphocyte activation in tumor-draining lymph nodes (**Fig. 6b-e, Extended Data Fig. 6h**). Although neutrophil frequencies were reduced, immune cell composition was largely comparable between control and COX-2 ko tumors at early disease stages (**Extended Data Fig. 6i**). We next performed scRNA-Seq to assess the impact of PGE_2 on the pancreatic TME. We observed marked gene expression changes in selected cell populations, such as macrophages, activated T cells and fibroblasts. More specifically, IL-1β$^+$ TAMs isolated from COX-2 ko tumors showed reduced expression of key identity genes and inflammatory response markers while acquiring IFN response signatures (**Fig. 6f-h**, **Extended Data Fig. 6j-l, Supplementary Table 6**). COX-2 ko tumors were however controlled in mice lacking a key subunit of the IFN-α/β receptor (*Ifnar1*$^{-/-}$) (**Extended Data Fig. 6m**). These data identify a key role of tumor-derived PGE_2 in driving the IL-1β$^+$ TAM state *in vivo* and show that targeting COX-2 leads to TME reprogramming and disease control in an IFN-independent manner.

IL-1β signaling in PDAC cells promotes tumor growth.

Antibody-mediated targeting of IL-1β *in vivo* led to delayed PDAC growth, concomitant with reduced expression of IL-1β by monocytes and TAMs, and with increased activation of cytotoxic T cells in draining lymph nodes (**Fig. 7a-c, Extended Data Fig. 7a-b**). Re-analysis of patient scRNA-Seq data highlighted tumor monocytes and *IL1B*$^+$ TAMs as the major sources of IL-1β, with subsets of dendritic cells and neutrophils expressing much lower transcript levels (**Extended Data Fig. 7c, Supplementary Table 1**). To determine the cellular targets of IL-1β in PDAC, we performed tumor challenge experiments in haemato-chimeric mice in which bone marrow (BM) cells from *Il1r1*$^{-/-}$ donors, which lack a key signaling subunit of the IL-1 receptor, or from wild-type control were transplanted into irradiated wild-type or *Il1r1*$^{-/-}$ recipients, respectively. No defect in tumor growth was observed in the two groups (**Extended Data Fig.**

7d), indicating that the cancer-promoting effects of IL-1β are not driven by signaling in hematopoietic or stromal cells. Instead, IL-1R1 ko KPC cells showed drastically reduced capacity to form tumors in immune competent mice, concomitant with reduced infiltration of IL-1β$^+$ monocytes and increased activation of CD8$^+$ T cells (**Fig. 7d-g, Extended Data Fig. 7e-g, Supplementary Table 7**). Re-expression of IL-1R1 in gene-targeted PDAC cells rescued tumorigenic potential *in vivo* (**Fig. 7h, Extended Data Fig. 7h**). Finally, stimulation with IL-1β promoted organoid generation by control – not by IL-1R1 ko – PDAC cells, and explants of IL-1R1 ko tumors showed defective organoid-forming efficiency (**Fig. 7i-j**). These data highlight a requirement for tumor cell-intrinsic IL-1β signaling for PDAC growth.

IL-1β signaling in PDAC cells sustains TAM recruitment and conditioning.

RNA-Seq analyses of KPC cells treated with IL-1β revealed marked up-regulation of genes encoding for myeloid growth factors (*Csf1*, *Csf2*), chemokines (*Ccl2*), cytokines (*Tnfa*), as well as for enzymes with immune regulatory functions (*Ptgs2*, *Nos2*) (**Extended Data Fig. 7i, Supplementary Table 7**). These results were confirmed by quantification of proteins in the supernatant of tumor cells, with CCL2 and CSF-1 being robustly induced upon IL-1β treatment (**Extended Data Fig. 7j)**. To assess the functional relevance of these molecules, we performed tumor challenge experiments in *Ccr2*$^{-/-}$ mice, which lack the CCL2 receptor, or in wild-type mice treated with a neutralizing antibody against CSF-1. Both experiments led to impaired disease growth, highlighting a key role of monocyte-derived macrophages in PDAC (**Extended Data Fig. 7k-l)**. We next focused on IL-1β-induced factors driving macrophage conditioning. Among the most enriched GO terms in the transcriptome of cytokine-treated tumor cells were inflammation and prostaglandin secretion, in line with the finding that stimulation of KPC cells with IL-1β led to increased production of PGE_2 and TNF-α (**Extended Data Fig. 7j, m-n, Supplementary Table 7**). We next performed supernatant transfer experiments whereby

tumor-conditioned media (TCM) from KPC cells treated with IL-1β in the absence or presence of COX-2 inhibitor (COX-2i) were incubated with a blocking antibody against TNF-α and subsequently transferred onto BMDMs. While TCM from untreated KPC cells (KPC^{UT}) did not trigger *Il1b* in macrophages, this gene was induced in response to TCM of IL-1β-stimulated tumor cells ($KPC^{IL\text{-}1\beta}$) (**Extended Data Fig. 7o**). Inhibition of COX-2 in KPC cells treated with IL-1β ($KPC^{IL\text{-}1\beta+COX\text{-}2i}$) led to lower induction of *Il1b* in BMDMs exposed to the corresponding TCM, with this occurrence being even more evident upon neutralization of TNF-α (**Extended Data Fig. 7o**). These data highlight a self-sustaining loop between PDAC cells and macrophages, in which IL-1β signaling in tumor cells triggers the release of factors that recruit monocytes to tumors and elicit the IL-1β^+ TAM state at least in part through PGE_2 and TNF-α.

Inflammatory reprogramming occurs early during pancreatic tumorigenesis

We integrated RNA-Seq data from cytokine-treated PDAC cells and organoids to define a tumor-intrinsic IL-1β response signature (T1RS) (**Fig. 8a, Extended Data Fig. 8a, Supplementary Table 8**). This gene module was enriched in mouse[18] and human[37] PDAC transcriptomes, and it correlated with predicted abundance of IL-1β^+ TAMs and with poor patient survival in TCGA data (**Fig. 8b-c, Extended Data Fig. 8b-c, Supplementary Table 8**). Longitudinal scRNA-Seq analyses of orthotopic mouse models revealed T1RS up-regulation in tumor cells at early time points, anticipating exponential disease growth and acquisition of proliferation, epithelial-to-mesenchymal transition (EMT), and extracellular matrix (ECM) remodeling programs (**Extended Data Fig. 8d-e**). To assess inflammatory reprogramming of tumor cells *in vivo*, we analyzed gene expression data from mouse models of pancreatic tumorigenesis[38]. These studies revealed highest T1RS expression in cells from mice with benign pancreatic intraepithelial neoplasia (PanIN), with levels of the signature

remaining elevated in established PDAC and distal metastasis (**Fig. 8d**). Spatial transcriptome data from donor and patient samples[39] confirmed robust expression of the T1RS genes in human PanIN and PDAC lesions (**Fig. 8e**). Inflammatory responses to tissue damage functionally cooperate with oncogenes to enhance pancreatic tumorigenesis via long-term reprogramming of epithelial cells[17,18]. In this context, we detected a subset of macrophages from patients with hereditary or idiopathic chronic pancreatitis[40] displaying a gene expression program analogous to that of IL-1β$^+$ TAMs (**Fig. 8f-g, Extended Data Fig. 8f**). Analysis of RNA-Seq data of normal or *Kras*-mutated cells from mice with cerulein-driven pancreatitis revealed marked T1RS expression as a consequence of oncogene activation, with levels of the module further increasing by injury (**Fig. 8h)**. Analogous findings were obtained in cells from mice treated with the alarmin IL-33, which mediates tissue damage responses in the pancreas[18] (**Fig. 8i)**. Furthermore, T1RS expression remained elevated in pancreatic spheroids generated from cerulein-treated mice months after resolution of the injury[17] (**Fig. 8j)**. We conclude that inflammatory reprogramming is an early event in pancreatic tumorigenesis, leading to persistent transcriptional changes that associate with disease progression and poor patient outcome.

IL-1β$^+$ TAMs spatially colocalize with T1RS$^+$ PDAC cells in patients.

We next asked whether local interactions with IL-1β$^+$ TAMs underlie transcriptional heterogeneity and inflammatory reprogramming of tumor cells. Analysis of patients scRNA-Seq data uncovered a subset of cancer cells expressing high levels of the T1RS (**Fig. 9a-b, Supplementary Table 9)**. Pseudotime analyses[41] identified these T1RS$^+$ PDAC cells as end points of a transcriptional trajectory driven by increasing expression of the T1RS itself and of known IL-1β target genes, such as *NFKBIA*, *IL1RN*, and *CXCL1* (**Fig. 9c-e, Supplementary Table 9)**. The predicted development of T1RS$^+$ PDAC cells was also associated with increased

expression of known tumor markers (*CEACAM6*, *CEACAM7*, *KRT19*) and with enrichment of GO terms associated to pancreatic tumorigenesis – Kras signaling, hypoxia, EMT, p53 pathway, and TGF-β signaling, among others (**Fig. 9e-f, Supplementary Table 9)**. These data highlight an intrinsic correlation between inflammatory reprogramming and acquisition of pathogenic programs by tumor cells. To assess the role of macrophages in this process, we performed single-cell spatial gene expression analyses in human PDAC samples. Highly multiplexed *in situ* RNA hybridization[42] with a custom panel of 98 gene probes identified IL-1β$^+$, FOLR2$^+$ and SPP1$^+$ TAMs, as well as subsets of tumor, epithelial, stromal, and immune cells; co-expression of *CXCL1* and *KRT19* was used as proxy to detect T1RS$^+$ PDAC cells (**Fig. 9g, Extended Data Fig. 9a-b, Supplementary Table 9)**. We observed marked spatial co-expression of *CXCL1* with *KRT19* and transcripts marking macrophages (*CD68*), IL-1β (*IL1B, IL1A, THBS1*) and PGE_2 (*PTGS2, PTGER1*) programs. Correlation values were indeed higher for marker genes of IL-1β$^+$ TAMs as compared to other subsets (**Fig. 9h**, **Extended Data Fig. 9c, Supplementary Table 9)**. We next set out to elucidate local cellular interactions between macrophages and tumor cells. Notably, T1RS$^+$ PDAC cells and IL-1β$^+$ TAMs were significantly and selectively enriched in each other's spatial neighborhoods **(Fig. 9i-j, Extended Data Fig. 9d-e)**. Ligand-receptor interactions analysis[43] between tumor cells and IL-1β$^+$ TAMs identified the IL-1:IL-1R1 axis as the top-ranking driver of T1RS$^+$ PDAC cell gene expression (**Fig. 9k-l, Extended Data Fig. 9f-i)**. These data highlight a spatially confined cross-talk between IL-1β$^+$ TAMs and T1RS$^+$ PDAC cells sustained by the PGE_2-IL-1β axis.

IL-1β$^+$ TAMs underlie pathogenic inflammation in a context-dependent manner.

We next set out to determine whether an IL-1β-dependent inflammatory loop between macrophages and tumor cells occurs in human cancer other than PDAC. By re-analyzing published scRNA-Seq datasets (see Methods), we identified IL-1β$^+$ TAMs in human

hepatocellular carcinoma, lung adenocarcinoma, glioblastoma, as well as in colorectal, breast and renal cancer (**Extended Data Fig. 10a-c, Supplementary Table 10**). Enrichment of the IL-1β$^+$ TAM signature in TCGA data correlated with poor patient survival of lung, renal, liver and brain cancers, while no significant association was observed for breast cancer and microsatellite-stable colorectal cancer. In contrast, the IL-1β$^+$ TAM signature correlated with good prognosis of patients with microsatellite-instable colorectal cancer (**Fig. 10a-c**). Analogous to what we observed in PDAC, patients with high expression of the IL-1β$^+$ TAM signature displayed elevated levels of T1RS (**Fig. 10d**). We conclude that IL-1β$^+$ TAMs are conserved across human cancers, and that their abundance correlates with IL-1β-driven inflammation and, in a context-dependent manner, with patient survival.

Discussion

We report a spatially confined and specific cross-talk between IL-1β$^+$ TAMs – a population of macrophages enriched in inflammatory but not cytotoxic programs – and a subset of PDAC cells expressing an IL-1β response signature (T1RS) associated with poor survival. Our data support a model whereby infiltrating monocytes are conditioned by cancer cell-derived PGE_2 and TNF-α and differentiate into IL-1β$^+$ TAMs. In turn, IL-1β triggers inflammatory reprogramming of neighboring PDAC cells and stimulates production of PGE_2, TNF-α and other factors that reinforce the IL-1β$^+$ TAM state. Elicitation of a positive feedback loop between IL-1β$^+$ TAMs and T1RS$^+$ PDAC cells supports locally elevated synthesis of PGE_2, and other inflammatory mediators whose activities are exerted over short distances[44,45], and it enables the maintenance of a functional TME niche. On the other hand, the self-sustaining nature of this interplay likely hinders its therapeutic targeting advanced disease. Our data highlight the PGE_2-IL-1β axis as a driver of the spatial and transcriptional heterogeneity of

338 immune and tumor cells whose early interference in patient at risk may have relevance for the
339 treatment of pancreatic cancer.

340 The biological effects of PGE_2 – suppression of cytotoxic immunity and enhancement of
341 tumor-promoting inflammation[46] – reflect divergent control of gene modules in macrophages.
342 PGE_2 limits IFN responses by targeting MEF2A and promoting IL-10 release[35], while boosting
343 expression of inflammatory factors with roles in tissue repair, such as IL-1β. The molecular
344 mechanisms underlying PGE_2-mediated synergisms remain to be elucidated. We found that IL-
345 $1\beta^+$ TAMs accumulate in hypoxic areas of the tumor where inflammation, tissue repair and
346 immune suppression co-exist[47]. In this context, PGE_2 was found to stabilize hypoxia-inducible
347 factor-1α (HIF-1α)[48], a transcription factor driving IL-1β synthesis in macrophages[49]. Future
348 studies should elucidate whether and how hypoxia or other factors, such as physical tension or
349 local interaction with stromal cells such as fibroblasts[50], contribute to the establishment or
350 maintenance of IL-$1\beta^+$ TAM niches.

351 Inflammatory signaling in epithelial cells sustains tissue repair but can enhance
352 tumorigenesis upon oncogene activation[17,18]. Reciprocally, driver mutations that accumulate in
353 healthy tissues may never give rise to tumors in the absence of sustained injury[16]. We found
354 that macrophages from pancreatitis patients acquire a gene expression program analogous to
355 that of IL-$1\beta^+$ TAMs, likely sustained by PGE_2 released from damaged cells[51]. Furthermore,
356 *Kras* mutations are sufficient to trigger PGE_2 synthesis[33] and T1RS expression in epithelial
357 cells at levels that are increased upon tissue injury. In this view, elicitation of a self-feeding
358 loop via the PGE_2-IL-1β axis would integrate and stabilize the consequences of tissue injury
359 and activated oncogenes. The pathogenic effects of inflammation in mutated cells underlie
360 processes as diverse as resurgence of stem cell programs, lineage infidelity or increased cell
361 fitness[16]. Inflammatory reprogramming of PDAC was required for disease growth and organoid
362 formation, and it was associated to the acquisition of pathologic programs such as EMT, in

keeping with recent reports in kidney cancer[52,53]. We posit that the PGE_2-IL-1β represents as a physiological response to injury whose cooptation by cancer promotes disease progression.

Our study and those of others[54-56] establish IL-1β as a common driver of pathogenic inflammation in cancer. We identified IL-1β^+ TAMs in multiple human tumors and linked the predicted abundance of these cells with high T1RS expression levels and poor patient prognosis in lung, kidney, liver and brain cancer. IL-1β^+ TAMs were instead associated with good outcome of patients with microsatellite-instable colorectal carcinoma, suggesting that inflammation may sustain protective responses in selected immunogenic diseases. We anticipate that targeting IL-1β or its receptor might yield variable therapeutic outcomes, according to the cell type- and tissue-specific activities of this cytokine[57]. Indeed, IL-1β production by hyperactive DC in tumor-draining lymph nodes was shown in support activation of cytotoxic T cells and elicitation of antitumor immunity[58]. Furthermore, the cardiovascular prevention trial CANTOS in patients treated with the anti-IL-1β antibody canakinumab showed a reduced incidence of lung cancer, but not of colon cancer.

By resolving the spatial and molecular diversity of TAMs in pancreatic cancer, we have elucidated the molecular regulation, functional outcomes, and key mechanisms of actions of the PGE_2-IL-1β axis. Our study should inform the design and interpretation of clinical trials that target IL-1β and/or COX-2 as preventive or combination immunotherapies[57,59,60].

REFERENCES

1 Halbrook, C. J., Lyssiotis, C. A., Pasca di Magliano, M. & Maitra, A. Pancreatic cancer: Advances and challenges. *Cell* **186**, 1729-1754, doi:10.1016/j.cell.2023.02.014 (2023).

2 Chen, D. S. & Mellman, I. Elements of cancer immunity and the cancer-immune set point. *Nature* **541**, 321-330, doi:10.1038/nature21349 (2017).

3 Bleriot, C., Chakarov, S. & Ginhoux, F. Determinants of Resident Tissue Macrophage Identity and Function. *Immunity* **52**, 957-970, doi:10.1016/j.immuni.2020.05.014 (2020).

4 Glass, C. K. & Natoli, G. Molecular control of activation and priming in macrophages. *Nat Immunol* **17**, 26-33, doi:10.1038/ni.3306 (2016).

5 Amit, I., Winter, D. R. & Jung, S. The role of the local environment and epigenetics in shaping macrophage identity and their effect on tissue homeostasis. *Nat Immunol* **17**, 18-25, doi:10.1038/ni.3325 (2016).

6 Mantovani, A., Allavena, P., Marchesi, F. & Garlanda, C. Macrophages as tools and targets in cancer therapy. *Nat Rev Drug Discov*, doi:10.1038/s41573-022-00520-5 (2022).

7 Ren, X. *et al.* Insights Gained from Single-Cell Analysis of Immune Cells in the Tumor Microenvironment. *Annu Rev Immunol* **39**, 583-609, doi:10.1146/annurev-immunol-110519-071134 (2021).

8 Salmon, H., Remark, R., Gnjatic, S. & Merad, M. Host tissue determinants of tumour immunity. *Nat Rev Cancer* **19**, 215-227, doi:10.1038/s41568-019-0125-9 (2019).

9 Medzhitov, R. The spectrum of inflammatory responses. *Science* **374**, 1070-1075, doi:10.1126/science.abi5200 (2021).

10 Dvorak, H. F. Tumors: wounds that do not heal. Similarities between tumor stroma generation and wound healing. *N Engl J Med* **315**, 1650-1659, doi:10.1056/NEJM198612253152606 (1986).

11 Mulder, K. *et al.* Cross-tissue single-cell landscape of human monocytes and macrophages in health and disease. *Immunity* **54**, 1883-1900 e1885, doi:10.1016/j.immuni.2021.07.007 (2021).

12 Cheng, S. *et al.* A pan-cancer single-cell transcriptional atlas of tumor infiltrating myeloid cells. *Cell* **184**, 792-809 e723, doi:10.1016/j.cell.2021.01.010 (2021).

13 Natoli, G. & Ostuni, R. Adaptation and memory in immune responses. *Nat Immunol* **20**, 783-792, doi:10.1038/s41590-019-0399-9 (2019).

14 Sanin, D. E. *et al.* A common framework of monocyte-derived macrophage activation. *Sci Immunol* **7**, eabl7482, doi:10.1126/sciimmunol.abl7482 (2022).

15 Hegde, S. *et al.* Dendritic Cell Paucity Leads to Dysfunctional Immune Surveillance in Pancreatic Cancer. *Cancer Cell* **37**, 289-307 e289, doi:10.1016/j.ccell.2020.02.008 (2020).

16 Weeden, C. E., Hill, W., Lim, E. L., Gronroos, E. & Swanton, C. Impact of risk factors on early cancer evolution. *Cell* **186**, 1541-1563, doi:10.1016/j.cell.2023.03.013 (2023).

17 Del Poggetto, E. *et al.* Epithelial memory of inflammation limits tissue damage while promoting pancreatic tumorigenesis. *Science* **373**, eabj0486, doi:10.1126/science.abj0486 (2021).

18 Alonso-Curbelo, D. *et al.* A gene-environment-induced epigenetic program initiates tumorigenesis. *Nature* **590**, 642-648, doi:10.1038/s41586-020-03147-x (2021).

19 Maynard, A. *et al.* Therapy-Induced Evolution of Human Lung Cancer Revealed by Single-Cell RNA Sequencing. *Cell* **182**, 1232-1251 e1222, doi:10.1016/j.cell.2020.07.017 (2020).

20 Sharma, A. *et al.* Onco-fetal Reprogramming of Endothelial Cells Drives Immunosuppressive Macrophages in Hepatocellular Carcinoma. *Cell* **183**, 377-394 e321, doi:10.1016/j.cell.2020.08.040 (2020).

21 Casanova-Acebes, M. *et al.* Tissue-resident macrophages provide a pro-tumorigenic niche to early NSCLC cells. *Nature* **595**, 578-584, doi:10.1038/s41586-021-03651-8 (2021).

22 Zhang, L. *et al.* Single-Cell Analyses Inform Mechanisms of Myeloid-Targeted Therapies in Colon Cancer. *Cell* **181**, 442-459 e429, doi:10.1016/j.cell.2020.03.048 (2020).

23 Chakarov, S. *et al.* Two distinct interstitial macrophage populations coexist across tissues in specific subtissular niches. *Science* **363**, doi:10.1126/science.aau0964 (2019).

24 Dick, S. A. *et al.* Three tissue resident macrophage subsets coexist across organs with conserved origins and life cycles. *Sci Immunol* **7**, eabf7777, doi:10.1126/sciimmunol.abf7777 (2022).
25 Guilliams, M. *et al.* Spatial proteogenomics reveals distinct and evolutionarily conserved hepatic macrophage niches. *Cell*, doi:10.1016/j.cell.2021.12.018 (2022).
26 Nalio Ramos, R. *et al.* Tissue-resident FOLR2(+) macrophages associate with CD8(+) T cell infiltration in human breast cancer. *Cell* **185**, 1189-1207 e1125, doi:10.1016/j.cell.2022.02.021 (2022).
27 Montaldo, E. *et al.* Cellular and transcriptional dynamics of human neutrophils at steady state and upon stress. *Nat Immunol* **23**, 1470-1483, doi:10.1038/s41590-022-01311-1 (2022).
28 Hingorani, S. R. *et al.* Trp53R172H and KrasG12D cooperate to promote chromosomal instability and widely metastatic pancreatic ductal adenocarcinoma in mice. *Cancer Cell* **7**, 469-483, doi:10.1016/j.ccr.2005.04.023 (2005).
29 Schiebinger, G. *et al.* Optimal-Transport Analysis of Single-Cell Gene Expression Identifies Developmental Trajectories in Reprogramming. *Cell* **176**, 928-943 e922, doi:10.1016/j.cell.2019.01.006 (2019).
30 Lange, M. *et al.* CellRank for directed single-cell fate mapping. *Nat Methods* **19**, 159-170, doi:10.1038/s41592-021-01346-6 (2022).
31 Liu, Z. *et al.* Fate Mapping via Ms4a3-Expression History Traces Monocyte-Derived Cells. *Cell* **178**, 1509-1525 e1519, doi:10.1016/j.cell.2019.08.009 (2019).
32 Ostuni, R. *et al.* Latent enhancers activated by stimulation in differentiated cells. *Cell* **152**, 157-171, doi:10.1016/j.cell.2012.12.018 (2013).
33 Zelenay, S. *et al.* Cyclooxygenase-Dependent Tumor Growth through Evasion of Immunity. *Cell* **162**, 1257-1270, doi:10.1016/j.cell.2015.08.015 (2015).
34 Perkins, D. J. *et al.* Autocrine-paracrine prostaglandin E2 signaling restricts TLR4 internalization and TRIF signaling. *Nat Immunol* **19**, 1309-1318, doi:10.1038/s41590-018-0243-7 (2018).
35 Cilenti, F. *et al.* A PGE2-MEF2A axis enables context-dependent control of inflammatory gene expression. *Immunity*, doi:10.1016/j.immuni.2021.05.016 (2021).
36 Zaslona, Z. *et al.* The Induction of Pro-IL-1beta by Lipopolysaccharide Requires Endogenous Prostaglandin E2 Production. *J Immunol* **198**, 3558-3564, doi:10.4049/jimmunol.1602072 (2017).
37 Peng, J. *et al.* Single-cell RNA-seq highlights intra-tumoral heterogeneity and malignant progression in pancreatic ductal adenocarcinoma. *Cell Res* **29**, 725-738, doi:10.1038/s41422-019-0195-y (2019).
38 Burdziak, C. *et al.* Epigenetic plasticity cooperates with cell-cell interactions to direct pancreatic tumorigenesis. *Science* **380**, eadd5327, doi:10.1126/science.add5327 (2023).
39 Carpenter, E. S. *et al.* Analysis of Donor Pancreata Defines the Transcriptomic Signature and Microenvironment of Early Neoplastic Lesions. *Cancer Discov* **13**, 1324-1345, doi:10.1158/2159-8290.CD-23-0013 (2023).
40 Lee, B. *et al.* Single-cell sequencing unveils distinct immune microenvironments with CCR6-CCL20 crosstalk in human chronic pancreatitis. *Gut* **71**, 1831-1842, doi:10.1136/gutjnl-2021-324546 (2022).
41 Street, K. *et al.* Slingshot: cell lineage and pseudotime inference for single-cell transcriptomics. *BMC Genomics* **19**, 477, doi:10.1186/s12864-018-4772-0 (2018).
42 Guilliams, M. *et al.* Spatial proteogenomics reveals distinct and evolutionarily conserved hepatic macrophage niches. *Cell* **185**, 379-396 e338, doi:10.1016/j.cell.2021.12.018 (2022).
43 Browaeys, R., Saelens, W. & Saeys, Y. NicheNet: modeling intercellular communication by linking ligands to target genes. *Nat Methods* **17**, 159-162, doi:10.1038/s41592-019-0667-5 (2020).
44 Gong, Z. *et al.* Lung fibroblasts facilitate pre-metastatic niche formation by remodeling the local immune microenvironment. *Immunity* **55**, 1483-1500 e1489, doi:10.1016/j.immuni.2022.07.001 (2022).
45 Roulis, M. *et al.* Paracrine orchestration of intestinal tumorigenesis by a mesenchymal niche. *Nature* **580**, 524-529, doi:10.1038/s41586-020-2166-3 (2020).

46 Bonavita, E. *et al.* Antagonistic Inflammatory Phenotypes Dictate Tumor Fate and Response to Immune Checkpoint Blockade. *Immunity*, doi:10.1016/j.immuni.2020.10.020 (2020).

47 Sattiraju, A. *et al.* Hypoxic niches attract and sequester tumor-associated macrophages and cytotoxic T cells and reprogram them for immunosuppression. *Immunity*, doi:10.1016/j.immuni.2023.06.017 (2023).

48 Liu, X. H. *et al.* Prostaglandin E2 induces hypoxia-inducible factor-1alpha stabilization and nuclear localization in a human prostate cancer cell line. *J Biol Chem* **277**, 50081-50086, doi:10.1074/jbc.M201095200 (2002).

49 Tannahill, G. M. *et al.* Succinate is an inflammatory signal that induces IL-1beta through HIF-1alpha. *Nature* **496**, 238-242, doi:10.1038/nature11986 (2013).

50 Adler, M. *et al.* Principles of Cell Circuits for Tissue Repair and Fibrosis. *iScience* **23**, 100841, doi:10.1016/j.isci.2020.100841 (2020).

51 Hangai, S. *et al.* PGE2 induced in and released by dying cells functions as an inhibitory DAMP. *Proc Natl Acad Sci U S A* **113**, 3844-3849, doi:10.1073/pnas.1602023113 (2016).

52 Li, R. *et al.* Mapping single-cell transcriptomes in the intra-tumoral and associated territories of kidney cancer. *Cancer Cell* **40**, 1583-1599 e1510, doi:10.1016/j.ccell.2022.11.001 (2022).

53 Chittezhath, M. *et al.* Molecular profiling reveals a tumor-promoting phenotype of monocytes and macrophages in human cancer progression. *Immunity* **41**, 815-829, doi:10.1016/j.immuni.2014.09.014 (2014).

54 Das, S., Shapiro, B., Vucic, E. A., Vogt, S. & Bar-Sagi, D. Tumor Cell-Derived IL1beta Promotes Desmoplasia and Immune Suppression in Pancreatic Cancer. *Cancer Res* **80**, 1088-1101, doi:10.1158/0008-5472.CAN-19-2080 (2020).

55 Hill, W. *et al.* Lung adenocarcinoma promotion by air pollutants. *Nature* **616**, 159-167, doi:10.1038/s41586-023-05874-3 (2023).

56 Dmitrieva-Posocco, O. *et al.* Cell-Type-Specific Responses to Interleukin-1 Control Microbial Invasion and Tumor-Elicited Inflammation in Colorectal Cancer. *Immunity* **50**, 166-180 e167, doi:10.1016/j.immuni.2018.11.015 (2019).

57 Garlanda, C. & Mantovani, A. Interleukin-1 in tumor progression, therapy, and prevention. *Cancer Cell* **39**, 1023-1027, doi:10.1016/j.ccell.2021.04.011 (2021).

58 Zhivaki, D. *et al.* Inflammasomes within Hyperactive Murine Dendritic Cells Stimulate Long-Lived T Cell-Mediated Anti-tumor Immunity. *Cell Rep* **33**, 108381, doi:10.1016/j.celrep.2020.108381 (2020).

59 Bell, C. R. *et al.* Chemotherapy-induced COX-2 upregulation by cancer cells defines their inflammatory properties and limits the efficacy of chemoimmunotherapy combinations. *Nat Commun* **13**, 2063, doi:10.1038/s41467-022-29606-9 (2022).

60 Nikolos, F. *et al.* Cell death-induced immunogenicity enhances chemoimmunotherapeutic response by converting immune-excluded into T-cell inflamed bladder tumors. *Nat Commun* **13**, 1487, doi:10.1038/s41467-022-29026-9 (2022).

61 Carpenter, E. S. *et al.* Analysis of donor pancreata defines the transcriptomic signature and microenvironment of early pre-neoplastic pancreatic lesions. *bioRxiv*, doi:10.1101/2023.01.13.523300 (2023).

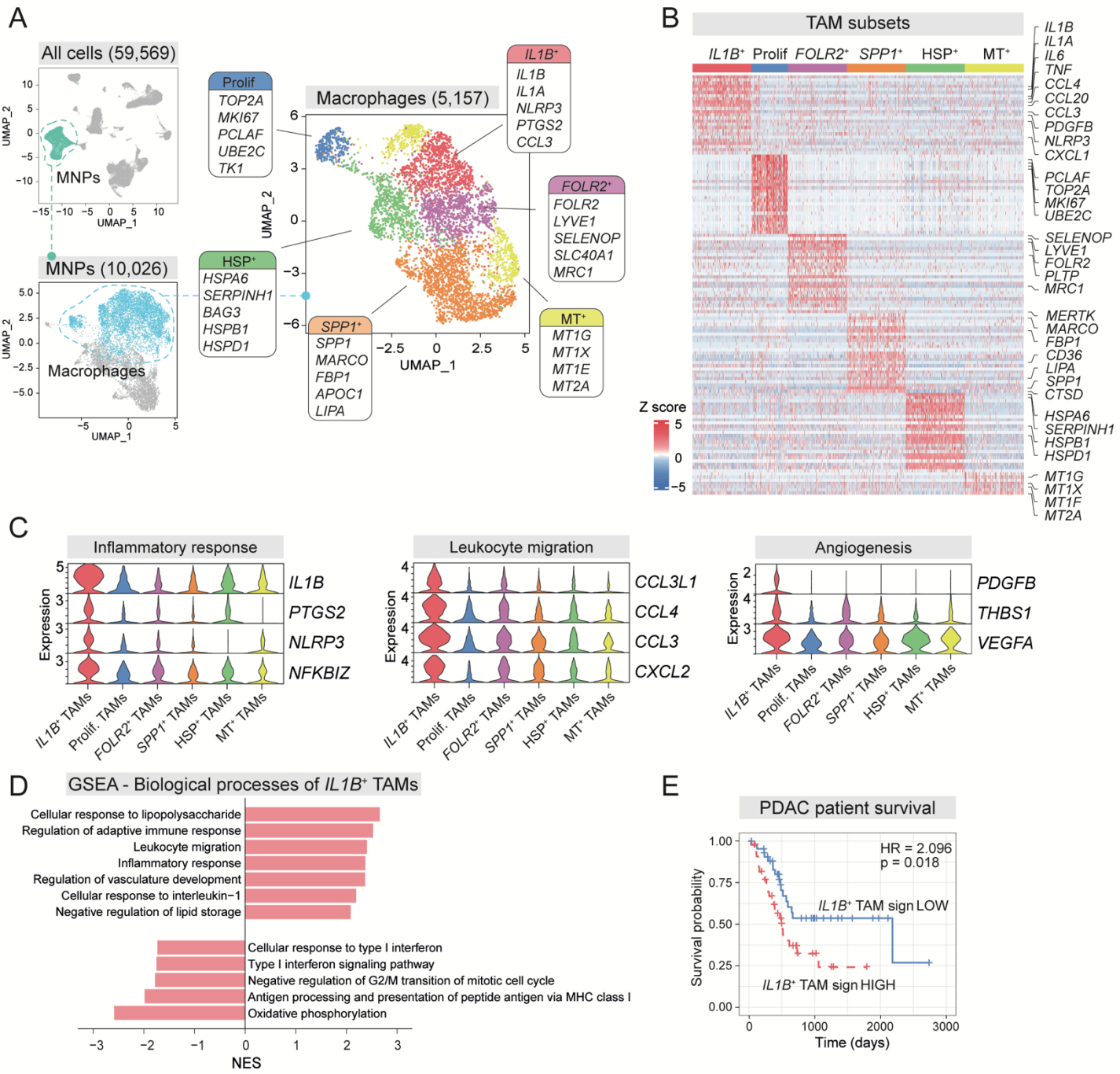

Fig. 1 | *IL1B*$^+$ TAMs correlate with poor prognosis in human PDAC. a) UMAPs of scRNA-Seq data from the complete dataset (upper left panel), mononuclear phagocytes (MNPs – lower left panel) and macrophages (right panel). Selected marker genes for each macrophage cluster are shown. **b)** Heatmap showing scaled gene expression of top 25 marker genes for each cluster of tumor-associated macrophages (ranked by $\log_2$FC). Relevant genes are shown. **c)** Violin plots showing expression values of selected genes associated to inflammatory response,

leukocyte migration and angiogenesis. **d)** Gene set enrichment analysis (GSEA) performed on all genes expressed by TAMs ranked by log_2FC between *IL1B*$^+$ TAMs and the other TAM clusters. Gene ontologies biological processes (GO BP) were used as gene sets. Normalized enrichment scores (NES) for relevant significant terms are reported. **e)** Kaplan-Meier plot showing survival probability of PDAC patients (TCGA), stratified based on expression (high or low) of the *IL1B*$^+$ TAM 6-gene prognostic signature (*IL1A, CCL20, CXCL3, IL1R2, EREG, PLAUR*), normalized by *CD68*. Hazard ratio (HR) and p-value of Cox regression fit are reported.

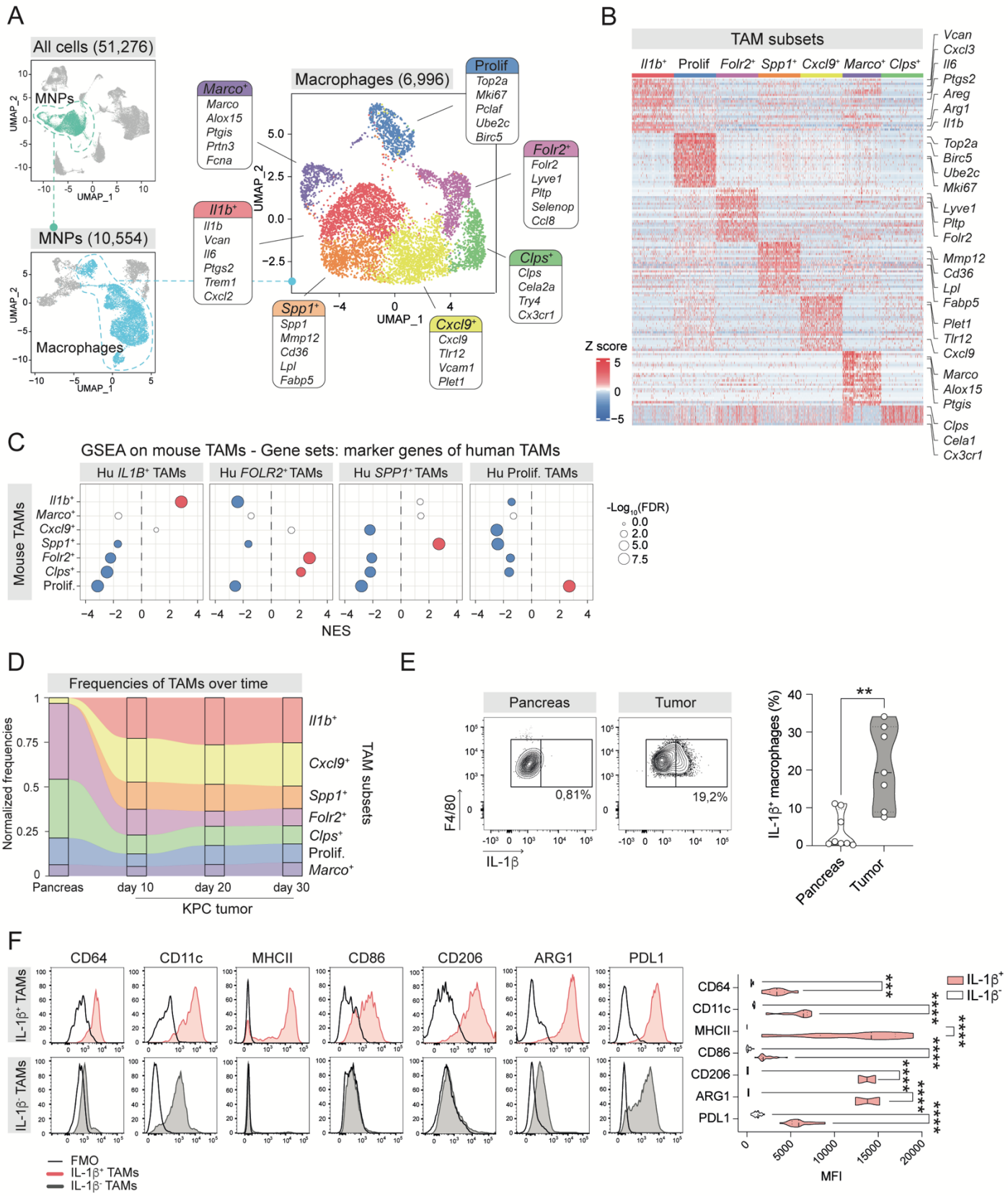

546 **Fig. 2 | IL-1β$^+$ TAMs are conserved in mouse models of pancreatic cancer. a)** UMAPs of

547 scRNA-Seq data from the complete dataset (upper left panel), mononuclear phagocytes (MNPs

548 – lower left panel) and macrophages (right panel). Relevant marker genes for each macrophage
549 cluster are shown. **b)** Heatmap showing scaled gene expression of top 25 marker genes for each
550 cluster of tumor-associated macrophages (ranked by log_2FC). Relevant genes are shown. **c)**
551 GSEA performed on genes expressed by mouse TAM subsets (ranked by Log_2FC vs other
552 TAM clusters), using the marker genes of human TAM subsets as gene sets. NES and
553 significance are reported for each comparison. Positive NES values are reported in red,
554 negative in blue and non-significant in white. **d)** Alluvial plot showing normalized frequencies,
555 calculated on scRNA-Seq data, of mouse TAM subsets at the indicated time points of tumor
556 growth. **e)** Representative contour plots and frequencies of mouse IL-1β^+ macrophages in
557 control pancreas (n=8) and tumor tissues (n=7). Statistical significance was measured by two-
558 tailed Student's t test. **$p < 0.01$. **f)** Expression of the indicated markers by IL-1β^+ TAMs
559 (upper panel, red histograms) and IL-1β^- TAMs (lower panel, grey histograms). Representative
560 histogram plots and median fluorescence intensity (MFI) values are shown. Black lines
561 represent fluorescence minus one control (FMO). Statistical significance was measured using
562 2-way ANOVA. ***$p < 0.001$, ****$p < 0.0001$.
563
564

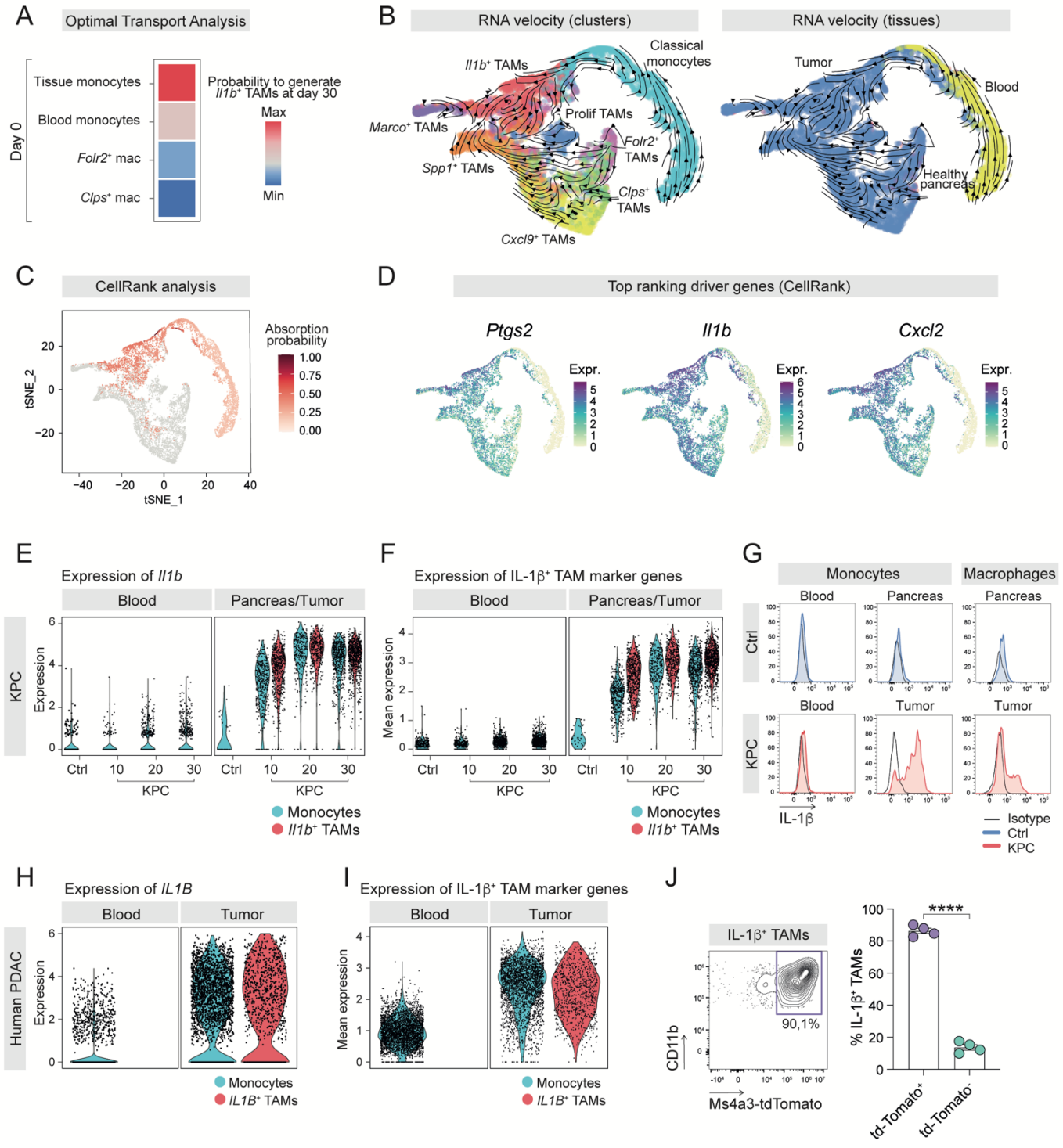

565 **Fig. 3 | Monocytes differentiate into IL-1β$^+$ TAMs upon exposure to TME factors. a)**

566 Heatmap showing fate probabilities to acquire *Il1b*$^+$ TAM identity (at day 30) for the indicated

567 populations (monocytes and macrophages at day 0), as computed by optimal transport analysis.

568 **b)** RNA velocity vectors of macrophages and monocytes from tissue and blood samples

computed on tSNE embedding based on diffusion maps. Cells are colored by cluster identity (left) or tissue of origin (right). **c)** Absorption probability towards *Il1b*$^{+}$ TAMs, identified as terminal state by CellRank. **d)** Expression values of the top-ranking genes driving the trajectory from monocytes towards *Il1b*$^{+}$ TAMs. **e, f)** Violin plots showing expression values of *Il1b* (**e**) and of marker genes conserved among human and mouse *Il1b*$^{+}$ TAMs (**f**), in mouse monocytes and *Il1b*$^{+}$ TAMs in the indicated conditions. **g)** Representative histogram plots of IL-1β intracellular staining of monocytes and macrophages in the indicated conditions. Cells from control mice are represented in blue, cells from tumor-bearing animals in red. Black lines represent isotype controls. **h, i)** Violin plots showing expression values of *IL1B* (**h**) and of marker genes conserved among human and mouse *Il1b*$^{+}$ TAMs (**i**) in human monocytes and *IL1B*$^{+}$ TAMs in blood and tumor samples from PDAC patients. **j)** Representative dot plot and frequencies of tdTomato^{+} and tdTomato^{-} IL-1β^{+} TAMs in end stage orthotopic tumors. Statistical analysis with unpaired student's two-tailed t test. ****$p<0.0001$.

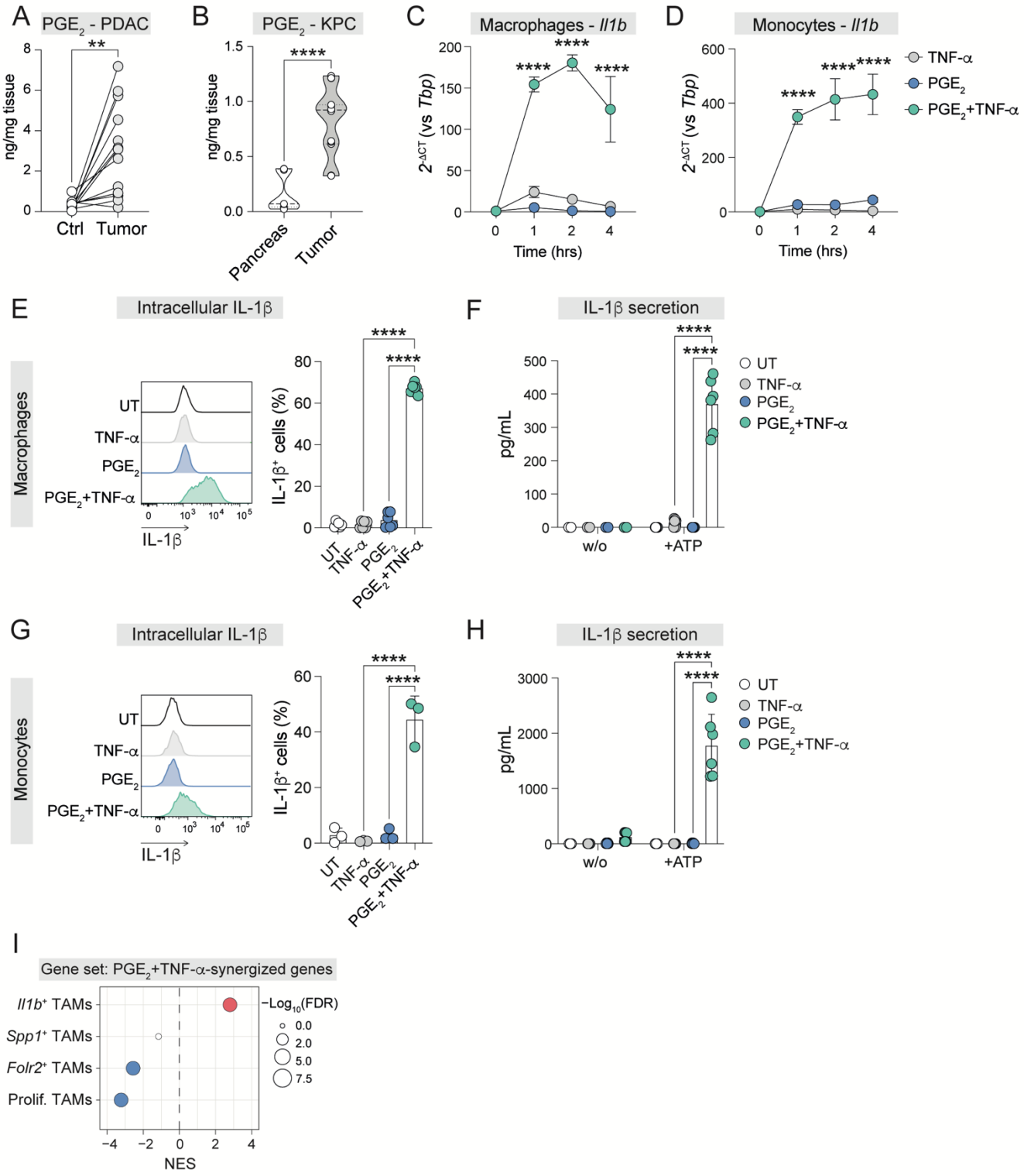

584 **Fig. 4 | PGE_2 and TNF-α cooperatively elicit the IL-1β$^+$ TAM state. a)** ELISA

585 quantification of PGE_2 in culture supernatant of human PDAC tissues (n=14) and matched

586 normal adjacent tissues (Ctrl) (n=14). Statistical significance was measured by Paired student's

two-tailed t test. ***p<0.001. **b)** Mass spectrometry quantification of PGE_2 in healthy pancreas (n=3) and end-stage KPC orthotopic tumors (n=5). Data reported are from three technical replicates for each sample. Statistical significance was measured by Unpaired student's two-tailed t test. ****p<0.0001. **c, d)** Real time qPCR analysis showing the expression of *Il1b* in bone marrow-derived macrophages (BMDMs) (**c**) and BM monocytes (**d**) stimulated *ex vivo* with TNF-α (10ng/mL); PGE_2 (1mM) or PGE_2+TNF-α for the indicated time points. Dot plots represent mean±SD (n=3). Data are representative of 3 independent experiments. Statistical significance was measured by two-way ANOVA. ****p<0.0001. **e, f)** Analysis of IL-1β production by BMDMs, as measured by intracellular staining (**e**) or by ELISA (**f**). BMDMs were stimulated either 6hrs, for intracellular staining of IL-1β, or 4hrs for quantification of secreted IL-1β. In the latter case, ATP was added for the last 30 minutes of stimulation. Bar plots represent the mean±SD (*n*=6) from two independent experiments. ****p<0.0001 calculated with ordinary one-way ANOVA (**e**) or two-way ANOVA (**f**). **g, h)** Analysis of IL-1β production by BM monocytes, as measured by intracellular staining (**g**) or by ELISA (**h**). Monocytes were stimulated either 5hrs, for intracellular staining of IL-1β, or 4hrs for quantification of secreted IL-1β. In the latter case, ATP was added for the last 30 minutes of stimulation. Bar plots represent the mean±SD (*n*=3). ****p<0.0001 calculated with ordinary one-way ANOVA (**g**) or two-way ANOVA (**h**). **i)** GSEA performed on genes expressed by mouse TAM subsets (ranked by log_2FC between each cluster and other TAM clusters), using PGE_2+TNF-α synergized genes as gene set. NES and significance are reported for each comparison. Positive NES values are reported in red, negative in blue and non-significant in white.

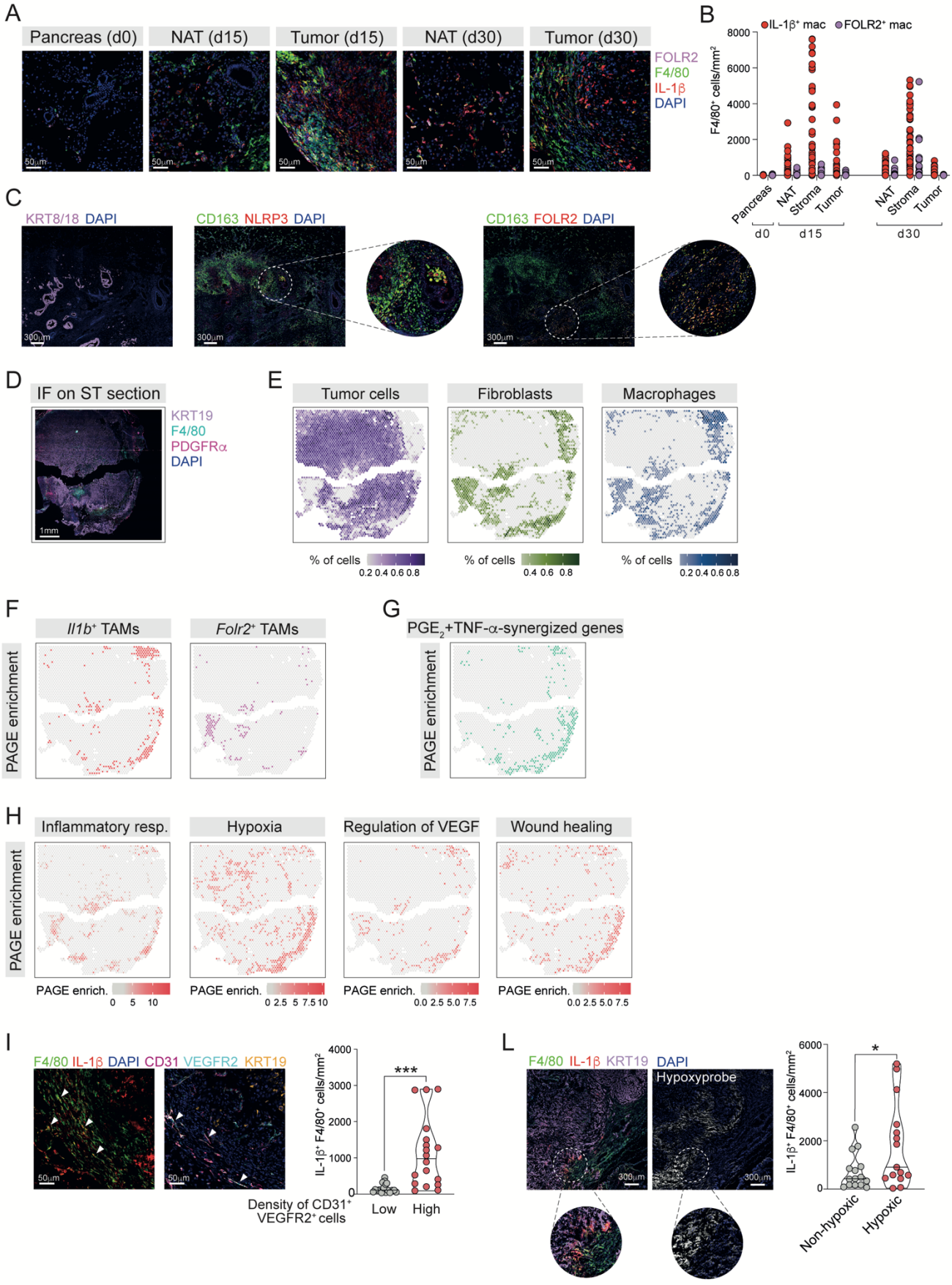

610 **Fig. 5 | IL-1β⁺ TAMs accumulate in areas of inflammation, hypoxia and angiogenesis. a)**

Representative immunofluorescence (IF) images of control pancreas (day 0) and murine PDAC samples and their normal adjacent tissue (NAT) at day 15 and day 30 p.i., stained for F4/80 (macrophages), IL-1β and FOLR2. **b)** Quantification of IL-1β$^+$ and FOLR2$^+$ macrophages/mm^2 in stroma, tumor compartment or NAT. **c)** Representative IF images of consecutive sections of human PDAC samples. Staining for KRT8-18 (tumor cells, left), CD163 (macrophages) and NLRP3 (middle), and CD163 and FOLR2 (right) is shown. **d)** IF staining on spatial transcriptomics (ST) section A1: KRT19 (tumor cells), F4/80 (macrophages), PDGFR-α (fibroblasts) and DAPI are shown. **e)** Percentages of tumor cells (left), fibroblasts (center) and macrophages (right) within each ST spot, as calculated by DestVI deconvolution. **f)** Parametric analysis of gene set enrichment (PAGE) of *Il1b*$^+$ (left) and *Folr2*$^+$ TAM marker genes (right). Macrophage-enriched ST spots with $p<0.001$ are shown. Significance was estimated considering all spots. **g)** PAGE of PGE_2+TNF-α synergized genes. ST spots with $p<0.001$ are shown. **h)** PAGE of genes belonging to the indicated GO BPs obtained by performing GSEA analysis on ST differentially expressed genes ranked by log_2FC between spots of cluster 4 and other spots (Seurat clustering in **Extended Data Fig. 5k)**. ST spots with $p<0.001$ are shown. **i)** Immunofluorescence (IF) analysis on consecutive sections of murine PDAC samples. Left: staining for F4/80 (macrophages) and IL-1β. Right: staining for CD31, VEGFR2 (endothelial cells) and KRT19 (tumor cells). Quantification of IL-1β$^+$ F4/80$^+$ cells in areas with high and low density of CD31$^+$ VEGFR2$^+$ cells (see Methods). Arrows indicate IL-1β$^+$ F4/80$^+$ cells (left) and CD31$^+$ VEGFR2$^+$ cells (right). **j)** Immunofluorescence (IF) analysis on consecutive sections of murine PDAC samples. Left: staining for F4/80 (macrophages), IL-1β and KRT19 (tumor cells); right: anti-Hypoxyprobe. Quantification of IL-1β$^+$ F4/80$^+$ cells in hypoxic and non-hypoxic areas (see Methods).

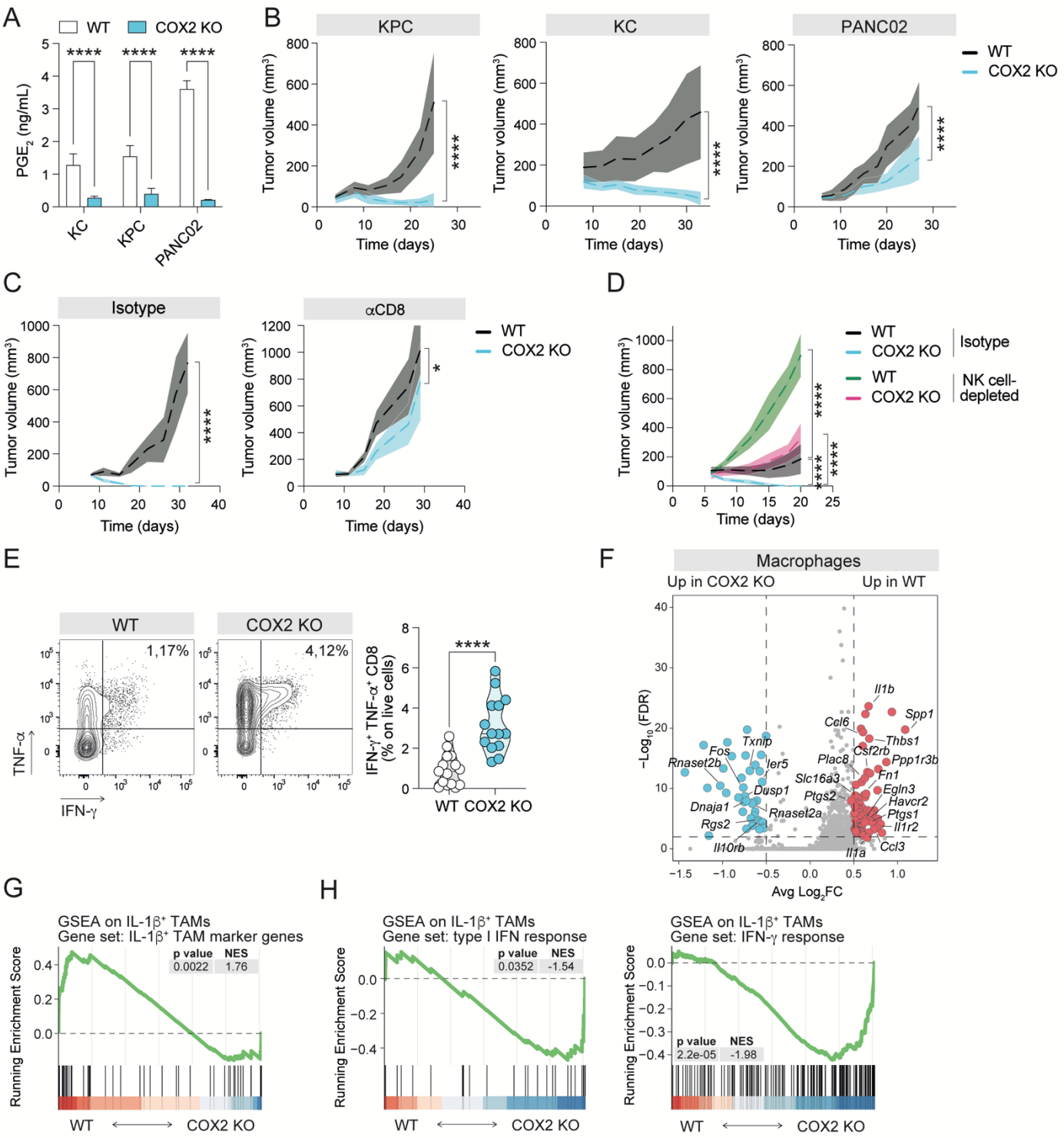

635 **Fig. 6 | PDAC-derived PGE_2 elicits IL-1β$^+$ TAMs and promotes tumor growth. a)**

636 Quantification by ELISA of PGE_2 produced by WT (n=≥3) and COX2 KO (n=≥3) PDAC

637 tumor cells cultured *in vitro* for 48hrs. Statistical significance was measured using 2-way

638 ANOVA. ****p < 0.0001. **b)** Growth curves of WT and COX2 KO KPC, KC and PANC02

inoculated subcutaneously in immune competent mice. Data are represented as mean±SD. *n*=10 mice/group. Statistical analysis was performed using two-way ANOVA. ****p < 0.0001. **c)** Growth curves of WT and COX2 KO KPC cells subcutaneously injected in immune competent mice treated with antibody targeting $CD8^+$ T cells or isotype control. Data are represented as mean±SD; *n*=5 mice/group. Statistical analysis was performed using two-way ANOVA. ****p < 0.0001, *p < 0.05. **d)** Growth curves of WT and COX2 KO KPC cells subcutaneously injected in immune competent mice treated with antibody targeting NK cells (αNK1.1+αASIALO GM-1) or isotype control. Data are represented as mean±SD; *n*=9 mice/group. Statistical analysis was performed using two-way ANOVA. ****p < 0.0001. **e)** Representative contour plots and quantification of IFN-γ^+ TNF-α^+ CD8 T cells in WT (*n*=15) and COX2 KO (*n*=14) tumor-draining lymph nodes (T-dLNs). Data represent 3 independent experiments. Significance was determined by unpaired t test. ****p < 0.0001. **f)** Volcano plot showing differentially expressed genes in WT (red) vs COX2-KO (blue) comparison within tumor-associated macrophages. Relevant genes are reported. **g, h)** GSEA performed on genes ranked by log_2FC in WT vs COX2-KO comparison of *Il1b*$^+$ TAMs, using (**g**) *Il1b*$^+$ TAM marker genes, (**h**) IFN-α-induced genes or IFN-γ-response genes (Hallmarks) as gene sets.

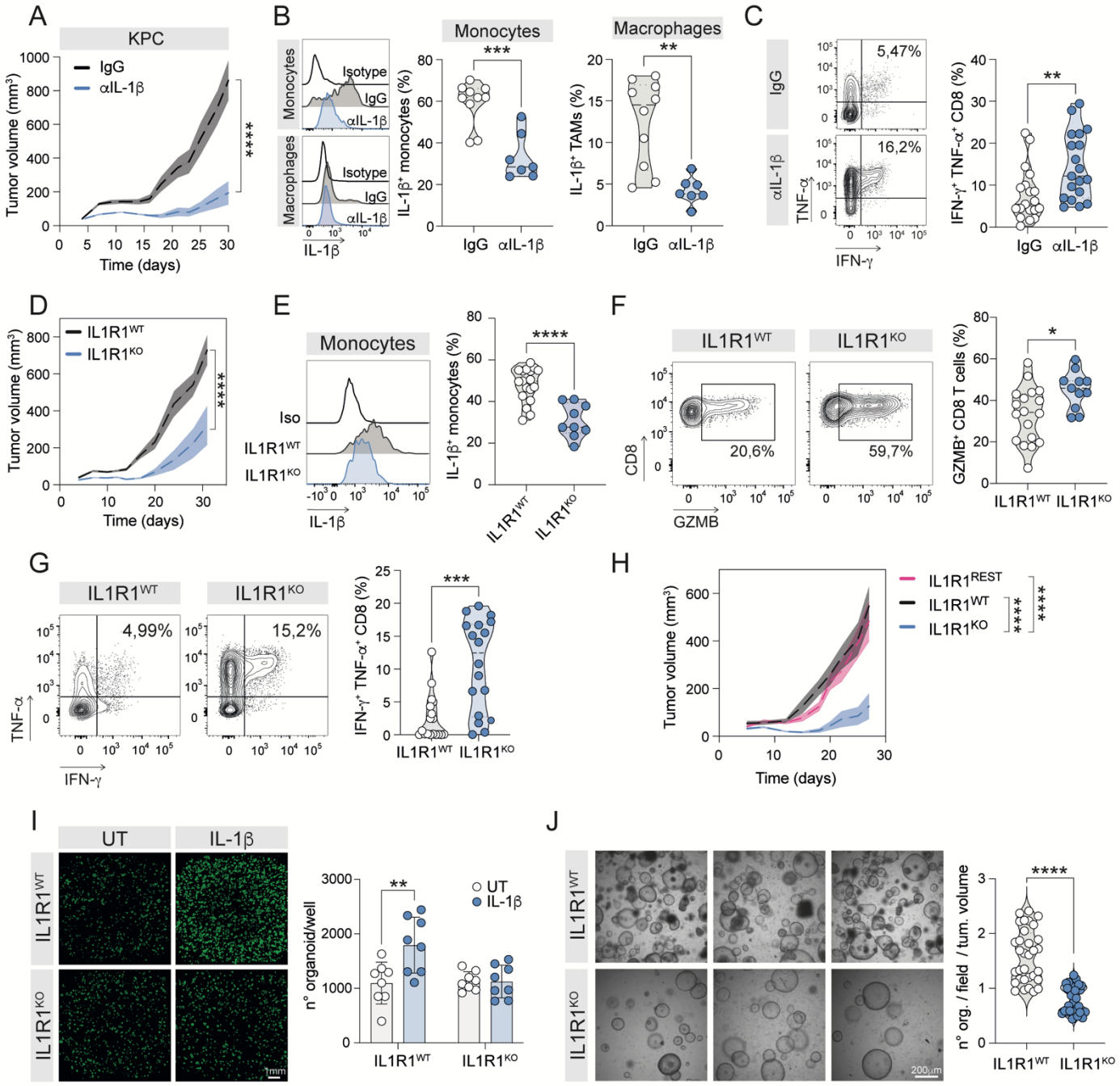

Fig. 7 | IL-1β signaling in PDAC cells is required for tumor growth. a) Growth curves of KPC cells inoculated subcutaneously in mice treated with anti-IL-1β (50μg/mouse, 3 times/week) or isotype control (IgG). Data are represented as mean±SEM. *n*=10 mice/group. Data are representative of 3 independent experiments. Statistical analysis with two-way ANOVA. ****p < 0.0001. **b)** Representative histogram plots and frequencies of IL-1β$^+$ monocytes (left) and IL-1β$^+$ macrophages (right) (IgG *n*=10; αIL-1β *n*=7). **p<0.01

661 ***p<0.001 (unpaired student's two-tailed t test). **c)** Flow cytometry analysis of tumor-
662 draining lymph nodes at day 30 p.i. upon *ex vivo* stimulation with PMA/Ionomycin and
663 Brefeldin A. Representative contour plots and frequencies of IFN-γ^+ TNF-α^+ CD8 T cells. Data
664 are from 2 independent experiments, *n*=19 mice/group. Statistical analysis with unpaired
665 student's two-tailed t test. **p<0.01. **d)** Growth curves of IL1R1^{WT} and IL1R1^{KO} PDAC cells
666 subcutaneously injected. Data represent mean±SEM (*n*=8 mice/group). Data are representative
667 of 2 independent experiments. Statistical analysis was performed using two-way ANOVA.
668 ****p<0.0001. **e, f)** Flow cytometry analysis of end stage IL1R1^{WT} and IL1R1^{KO} tumors.
669 n=7/18 IL1R1^{KO} tumors were rejected. Representative histograms and frequencies of IL-1β^+
670 monocytes **(e)** (IL1R1^{WT} *n*=18; IL1R1^{KO} *n*=9), or GZMB$^+$ CD8 T cells **(f)** (IL1R1^{WT} *n*=18;
671 IL1R1^{KO} *n*=11) are shown. Data are from 2 independent experiments. Statistical analysis was
672 performed using unpaired student's two-tailed t test. *p<0.05 ****p<0.0001. **g)** Flow
673 cytometry of tumor-draining lymph nodes upon *ex vivo* stimulation with PMA/Ionomycin with
674 Brefeldin A. Representative plots and frequencies of IFN-γ^+ TNF-α^+ CD8 T cells. Data are
675 from 2 independent experiments, *n*=18 mice/group. Statistical analysis was performed using
676 unpaired student's two-tailed t test. ***p<0.001. **h)** Growth curves of IL1R1^{WT}, IL1R1^{KO} or
677 IL1R1^{REST} PDAC cells inoculated subcutaneously. Data represent mean±SEM. *n*=10
678 mice/group. Significance was assessed by 2-way ANOVA, ****p<0.0001. **i)** Representative
679 images and quantification of IL1R1 WT and IL1R1 KO organoids treated with IL-1β for 5
680 days or left untreated (*n*=8 wells/condition; the entire Matrigel area was collected for each
681 well). Significance was assessed by 2-way ANOVA, **p<0.01. **j)** Organoid-forming efficiency
682 of IL1R1^{WT} and IL1R1^{KO} tumors explanted at day 11 post inoculation. Organoid numbers were
683 counted after 6 days of culture (4 fields/well were counted; each tumor (*n*=4/group) was plated
684 in 8 wells). Dots represent the mean number of organoids per field, normalized for tumor

685 volume. Significance was assessed by unpaired student’s two-tailed t test with Welch's
686 correction, ****$p<0.0001$.
687
688

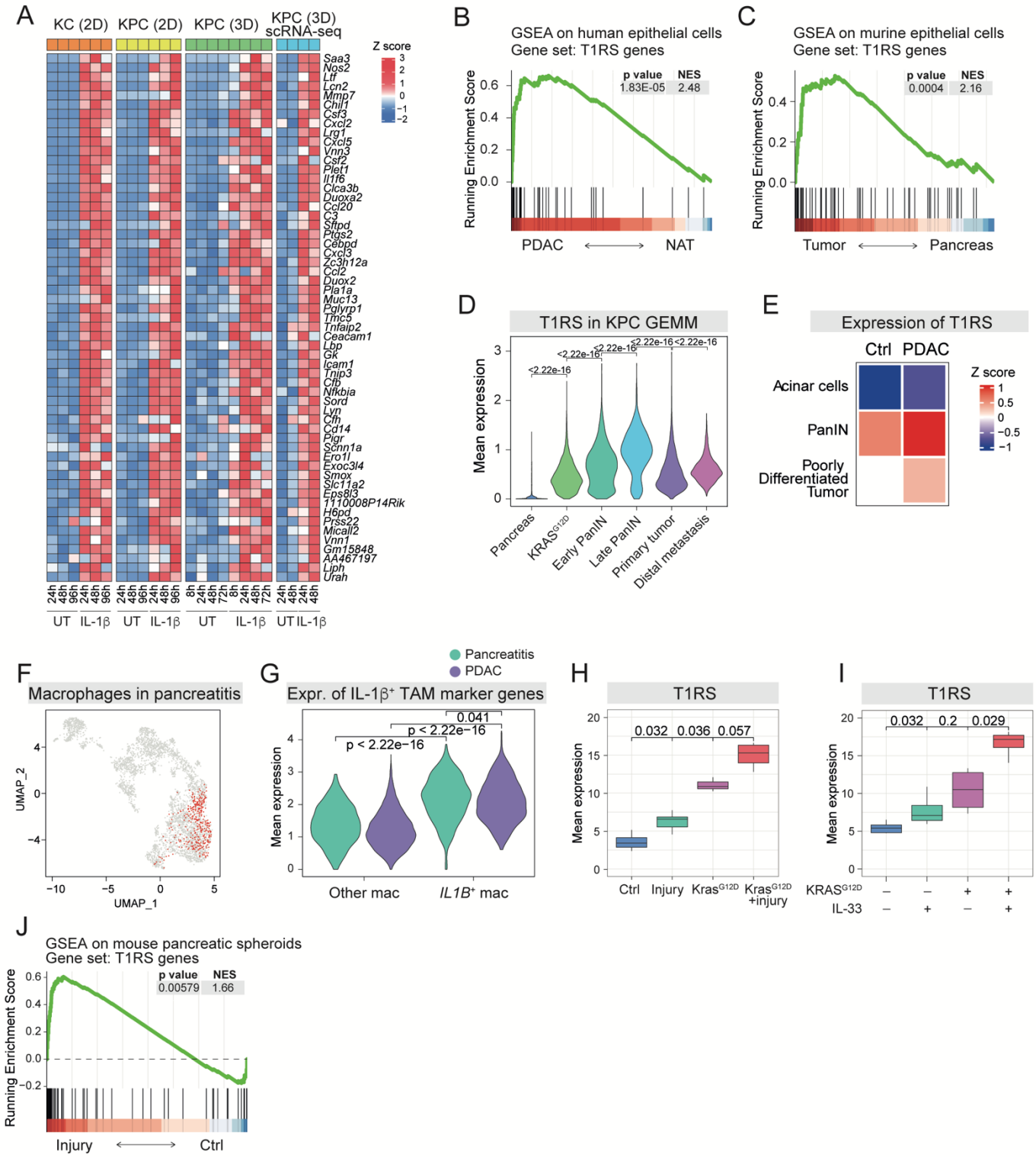

689 **Fig. 8 | Inflammatory reprogramming occurs early during pancreatic tumorigenesis. a)**

690 Heatmap showing scaled gene expression of the 57 genes composing T1RS in KC or KPC cells

691 stimulated with IL-1β or left untreated, in the indicated conditions and time-points. **b)** GSEA

692 performed on genes ranked by log_2FC between human malignant and non-malignant pancreatic

693 epithelial cells[37], using T1RS (human orthologs) as gene set. **c)** GSEA performed on genes
694 ranked by log_2FC in the comparison between murine malignant and non-malignant pancreatic
695 epithelial cells[18], using T1RS as gene set. **d)** Mean expression of T1RS in murine epithelial
696 cells at different stages of tumor progression[38]. **e)** Heatmap showing scaled mean expression
697 of T1RS (human orthologs) in GeoMX data performed on ROIs of healthy donors and PDAC
698 patients. ROI were annotated as acinar cells, PanIN and poorly differentiated tumor[61]. **f)** UMAP
699 of pancreatic macrophages from healthy donors and patients with pancreatitis[40]. *IL1B*$^+$
700 macrophages were annotated using the scRNA-Seq dataset of human TAMs as reference (**Fig.**
701 **1a, Supplementary Table 1**) and are highlighted in red. **g)** Mean expression of *IL1B*$^+$ TAM
702 marker genes in tissue macrophages from pancreatitis patients and PDAC patients. **h-i)** Box
703 plot showing mean expression of T1RS in murine pancreatic epithelial cells[18] with normal or
704 mutated *Kras* upon injury induced with caerulein **(h)** or after injection of IL-33 **(i)**. Significance
705 is computed by Mann-Whitney test. **j)** GSEA performed on genes ranked by log_2FC in the
706 comparison between spheroids obtained from pancreatic epithelial cells after *in vivo* resolution
707 of injury and spheroids obtained from healthy pancreatic epithelial cells[17]. T1RS was used as
708 gene set.

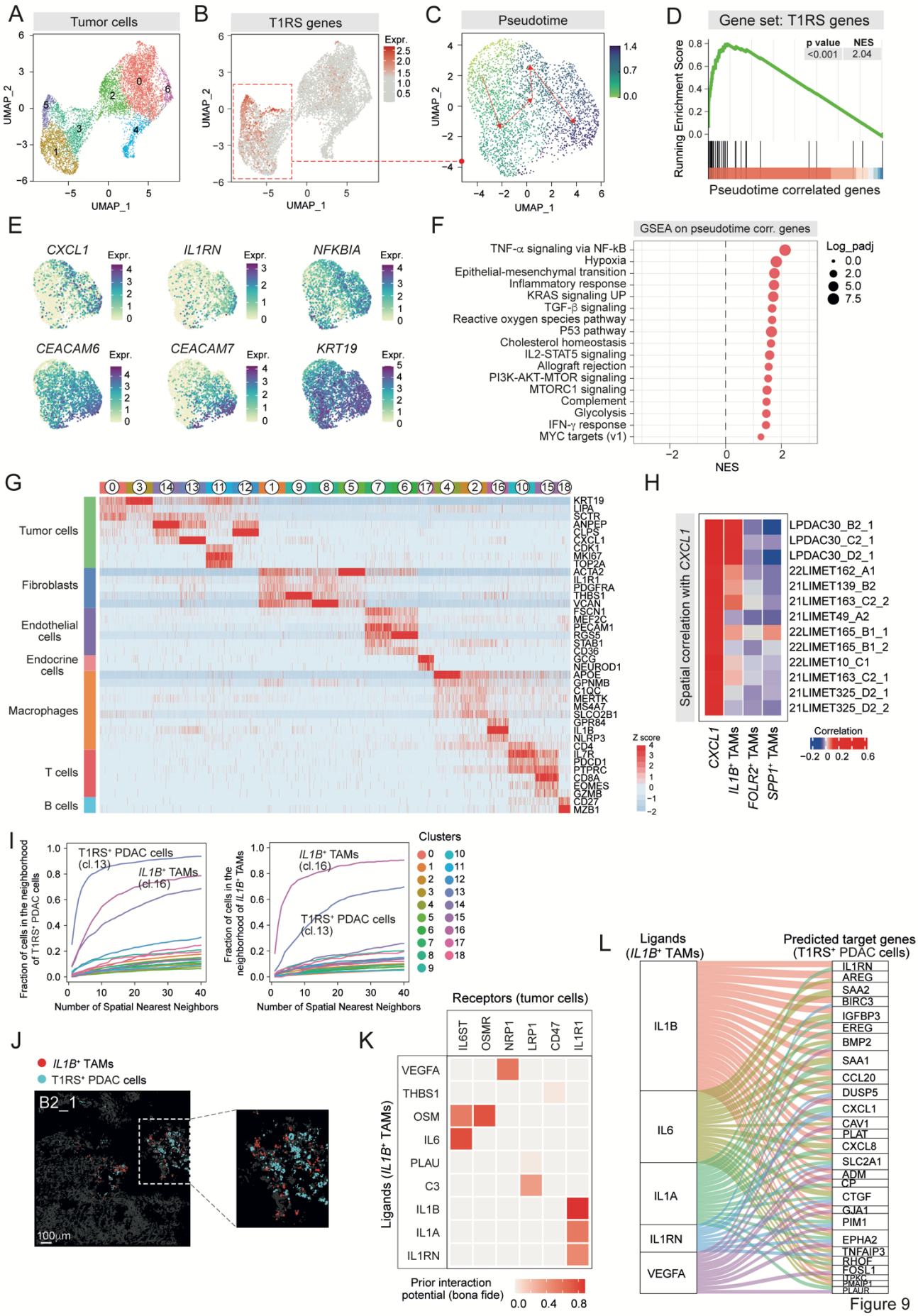
A
Tumor cells
UMAP_2
UMAP_1
B
T1RS genes
Expr.
C
Pseudotime
D
Gene set: T1RS genes
p value
NES
<0.001
2.04
Running Enrichment Score
Pseudotime correlated genes
E
CXCL1
IL1RN
NFKBIA
CEACAM6
CEACAM7
KRT19
Expr.
F
GSEA on pseudotime corr. genes
TNF-α signaling via NF-kB
Hypoxia
Epithelial-mesenchymal transition
Inflammatory response
KRAS signaling UP
TGF-β signaling
Reactive oxygen species pathway
P53 pathway
Cholesterol homeostasis
IL2-STAT5 signaling
Allograft rejection
PI3K-AKT-MTOR signaling
MTORC1 signaling
Complement
Glycolysis
IFN-γ response
MYC targets (v1)
Log_padj
NES
G
Tumor cells
Fibroblasts
Endothelial cells
Endocrine cells
Macrophages
T cells
B cells
Z score
H
Spatial correlation with CXCL1
LPDAC30_B2_1
LPDAC30_C2_1
LPDAC30_D2_1
22LIMET162_A1
21LIMET139_B2
21LIMET163_C2_2
21LIMET49_A2
22LIMET165_B1_1
22LIMET165_B1_2
22LIMET10_C1
21LIMET163_C2_1
21LIMET325_D2_1
21LIMET325_D2_2
CXCL1
IL1B+ TAMs
FOLR2+ TAMs
SPP1+ TAMs
Correlation
I
T1RS+ PDAC cells (cl.13)
IL1B+ TAMs (cl.16)
Fraction of cells in the neighborhood of T1RS+ PDAC cells
Fraction of cells in the neighborhood of IL1B+ TAMs
Number of Spatial Nearest Neighbors
Clusters
J
IL1B+ TAMs
T1RS+ PDAC cells
B2_1
100μm
K
Receptors (tumor cells)
IL6ST
OSMR
NRP1
LRP1
CD47
IL1R1
Ligands (IL1B+ TAMs)
VEGFA
THBS1
OSM
IL6
PLAU
C3
IL1B
IL1A
IL1RN
Prior interaction potential (bona fide)
L
Ligands (IL1B+ TAMs)
Predicted target genes (T1RS+ PDAC cells)
IL1B
IL6
IL1A
IL1RN
VEGFA
IL1RN
AREG
SAA2
BIRC3
IGFBP3
EREG
BMP2
SAA1
CCL20
DUSP5
CXCL1
CAV1
PLAT
CXCL8
SLC2A1
ADM
CP
CTGF
GJA1
PIM1
EPHA2
TNFAIP3
RHOF
FOSL1
PMAIP1
PLAUR

Figure 9

Fig. 9 | IL-1β$^+$ TAMs spatially colocalize with T1RS$^+$ PDAC cells in patients. a) UMAP showing clustering of tumor cells obtained from chemotherapy naïve PDAC samples. **b)** UMAP plot showing mean expression of T1RS genes (human orthologs) in tumor cells. **c)** UMAP plot showing trajectory and pseudotime computed on tumor cells from chemotherapy naïve PDAC samples. **d)** GSEA performed on the genes expressed by tumor cells ranked by correlation with pseudotime, using T1RS genes (human orthologs) as gene set. **e)** UMAPs showing expression of relevant genes with high correlation with pseudotime. **f)** GSEA performed on genes expressed in tumor cells ranked by correlation with pseudotime using MSigDB hallmark genes as gene sets. NES and significance are reported for each comparison. **g)** Heatmap showing scaled gene expression values of marker genes for each cluster shown in **Extended Data Fig. 9b**. **h)** Gene expression spatial correlation of marker genes of TAM subsets with *CXCL1* (see Methods). Mean spatial correlation is reported. **i)** Analysis of the fraction of cells that are present in the neighborhood of T1RS$^+$ tumor cells (left) and *IL1B*$^+$ TAMs (right), calculated for each cluster for increasing numbers of nearest neighbors. **j)** Snapshot of a representative region of interest (LPDAC30 B2_1) showing T1RS$^+$ tumor cells (light blue) and *IL1B*$^+$ TAMs (red). **k)** Heatmap showing interaction potential between the receptors expressed in tumor cells and the top ranked ligands expressed in *IL1B*$^+$ TAMs (predicted by NicheNet). **l)** Alluvial plot showing top 5 ligands expressed in *IL1B*$^+$ TAMs, ranked by their overall regulatory potential on target genes (see Methods). Predicted target genes are identified as marker genes of cluster 2, representing the endpoint of tumor cell trajectory (**Fig. 9c**, **Extended Data Fig. 9g**). Thickness of the lines connecting ligands and targets is proportional to regulatory potential.

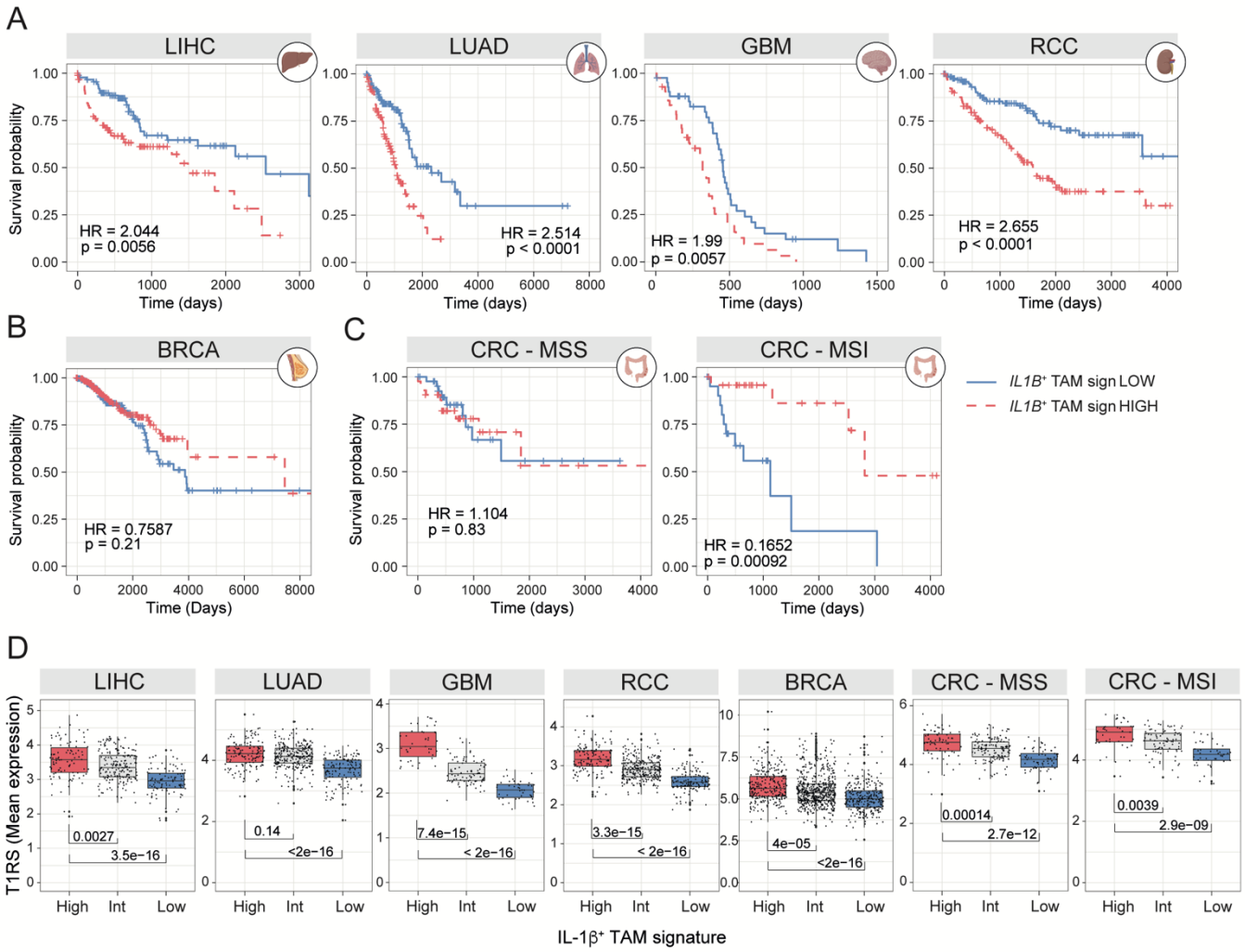

733 **Fig. 10 | IL-1β$^+$ TAMs underlie pathogenic inflammation in a context-dependent manner.**

734 **a-c)** Kaplan-Meier plot showing survival probability of different TCGA cohorts of solid

735 tumors: **a)** liver hepatocellular carcinoma (LIHC), lung adenocarcinoma (LUAD),

736 glioblastoma multiforme (GBM), renal clear cell carcinoma (RCC), **b)** breast invasive

737 carcinoma (BRCA) and **c)** colon adenocarcinoma (CRC). CRC patients were grouped as

738 microsatellite stable (MSS) and microsatellite instable (MSI). Patients from all the cohorts are

739 stratified in *IL1B*$^+$ TAM signature high (red) and low (blue) groups according to the expression

740 of *IL1B*$^+$ TAM prognostic signature (**Fig. 1e**). Hazard ratio (HR) and p-value of Cox regression

741 fit are reported. **d)** Box plot showing gene expression of T1RS genes (human orthologs) in

742 multiple TCGA cohorts of solid tumors. Patients are stratified according to the *IL1B*$^+$ TAM

743 prognostic signature (**Fig. 1e**). Significance is computed by Mann-Whitney test.

ACKNOWLEDGEMENTS

We thank Martino A. Cappelluti and Angelo Lombardo for help with CRISPR-Cas9 gene targeting experiments; Ganesh Bhat and Dario Bonanomi for help with IF analyses; Cecilia Garlanda (Humanitas Research Hospital) for providing *Il1r1*$^{-/-}$ mice; Gioacchino Natoli, Bruno Amati, Andres Hidalgo, Andrea Ditadi and all R.O. lab members for discussions and/or critical reading of the manuscript. We thank the following Centers and facilities of Ospedale San Raffaele: Center for Omics Sciences (COSR), Proteomics and Metabolomics Facility (ProMeFa), Flow cytometry Resource, Advanced Cytometry Technical Applications Laboratory (FRACTAL), Advanced Light and Electron Microscopy BioImaging Center (ALEMBIC); Preclinical Imaging Facility, Centro Risorse Biologiche (CRB-OSR); Centro Universitario di Statistica per le Scienze Biomediche (CUSSB) at Vita-Salute San Raffaele University. Figures were created with Adobe Illustrator and BioRender.com. F.M.V., L.M., and V.C. conducted this study as partial fulfilment of a PhD in Molecular Medicine at Vita-Salute San Raffaele University. F.L.T. and C.L. conducted this study as partial fulfilment of a PhD in Complex Systems for Quantitative Biomedicine at University of Turin. N.C. and E.M. received support by fellowships from Fondazione Umberto Veronesi (FUV). P.C and F.N. are supported by grants from the Italian Association for Cancer Research (AIRC) (IG 19931 and 26341) and Fondazione CRT (2019-1887 and 2020-0719). This study was supported by grants from the European Research Council (ERC) (ERC Starting Grant 759532, X-TAM, to R.O.), AIRC (MFAG 20247, Bridge Grant 27844, and AIRC 5x1000 special program 22737 to R.O.), and the Italian Ministry of Health (GR-201602362156, GR-2021-12374094 to R.O). Research in R.O. lab is supported by grants from the Italian Telethon Foundation (SR-Tiget Grant Award F04).

AUTHOR CONTRIBUTIONS

N.C., F.L.T., F.M.V., G.B. contributed to the design of the study, analyzed data, prepared figures and edited the manuscript; N.C. and F.M.V. performed or contributed to all experiments, with help from L.M., S. Barresi, E.M., E.D. A.C., M.S.F.N, S. Brugiapaglia, A.S., P. Cappello; F.L.T. and G.B performed all computational analyses, with help from C.L., E.L.; V. Cuzzola, M.G. performed spatial gene expression experiments, with help from M.S.L. and C.D.; M.P. and P. Canevazzi performed spheroid and organoid culture experiments; G.D. performed lineage tracing experiments; D.D and A.A. performed mass spectrometry analyses; S.C. and M.F. selected and recruited study participants; A. Mortellaro, V. Corbo, Z.L., A. Mondino provided resources; P.D., L.P., C.T., F.N., M.I., L.G.N., F.G., C.B., L.N. provided key scientific inputs. R.O. conceptualized and coordinated the study, acquired funding, analyzed the data and wrote the paper. All authors read and edited the manuscript.

DECLARATION OF INTERESTS

The authors declare no competing interests.

METHODS

Patient samples. Human samples from resected primary PDAC as well as peripheral blood (PB) samples were obtained from the Pancreatic Surgery Unit at the Pancreas Translational and Clinical Center of San Raffaele Hospital (Milan, Italy). The study was compliant with the Declaration of Helsinki and the General Data Protection Regulation and was approved by San Raffaele Hospital (protocols: NEU-IPMN and LiMeT). Tissue specimens were confirmed to be tumor or adjacent-normal tissue based on pathologist assessment. Informed consent was obtained by all participants, which received no compensation. Age and sex, as well as anonymized clinical information of participants are reported in **Supplementary Table 1**.

Mouse PDAC. KC (DT6606) and KPC (K8484) cell lines were previously established [1-3] from tumors arising in genetically engineered mouse models carrying the G12D oncogenic mutation in the *Kras* gene (*Kras*$^{LSL\text{-}G12D/+}$;*Pdx1*$^{Cre/WT}$ for KC) and the missense point R720H mutation in the *Tpr53* gene (*Kras*$^{LSL\text{-}G12D/+}$;*Tpr53*$^{LSL\text{-}R270H/+}$;*Pdx1*$^{Cre/WT}$ for KPC). Panc02 cell line is derived from a methylcholanthrene-induced pancreatic ductal adenocarcinoma[4]. KC, KPC and Panc02 cell lines were kindly provided by Piemonti L. All the cell lines were cultured under standard conditions, and periodically tested for mycoplasma.

CRISPR-Cas9-mediated gene targeting. Single guide RNAs (sgRNAs) were designed using CHOPCHOP [5] and synthetized by *in vitro* transcription using GeneArt™ Precision gRNA Synthesis Kit (Invitrogen), following manufacturer's instructions. Ribonucleoprotein complexes (RNPs: Cas9-sgRNA) were generated by incubating 12µg of sgRNA with 5µg of Cas9 for 15 min at RT. KPC, KC or Panc02 cells (2.5×10^4) were resuspended in SF solution of SF Cell Line 4D Nucleofector™ X Kit S, mixed with RNPs and electroporated using EP-100 program of the 4D-Nucleofector System (Lonza). Three days after nucleofection, single clones were FACS-sorted in 96 well plates. Single cell clones were screened to evaluate Non-Homologous End Joining (NHEJ) efficiency on the targeted site with T7 endonuclease assay.

Briefly, genomic DNA was extracted using QuickExtract™ DNA Extraction Solution and targeted regions were amplified by PCR. PCR products were purified with Ampure XP beads and quantified by Nanodrop 8000. Purified PCR products were mixed 1:1 with corresponding products from wild-type cells. Annealed PCR products (400 ng) were digested with T7 Endonuclease for 30 min at 37°C and subjected to capillary electrophoresis using D1000 TapeStation kit (Agilent 4200 TapeStation). NHEJ efficiency was defined by calculating the percentage of PCR product cleavage. Gene-edited clones were validated by Sanger Sequencing using PCR products encompassing the target sequence. Polyclonal KO pools were generated mixing an equal amount of at least 5 validated clones. The absence of the targeted protein was further validated by western-blot analyses. A complete list of sgRNAs and primer pairs used for the NHEJ assay is reported in the **Supplementary Table 6 and 7**.

***In vivo* animal studies.** All experiments and procedures were performed according to protocols approved by the Institutional Animal Care and Use Committee (IACUC) at San Raffaele Scientific Institute animal facilities and authorized by the Italian Ministry of Health in accordance with the Italian Laws (D.L.vo 116/92), which enforce the EU 86/609 Directive (approval number #449/2018-PR; #962/2020-PR and #908/2021-PR). C57BL/6N mice were purchased from Charles River Italy; IFNAR KO and CCR2 KO mice were obtained from Matteo Iannacone (IRCCS San Raffaele Scientific Institute, Milan, Italy); IL1R1 KO mice were kindly provided by Cecilia Garlanda (Humanitas Research Hospital, Milan, Italy). All animals were maintained under pathogen-free conditions at the animal facility of San Raffaele Scientific Institute. $Ms4a3^{CreERT2}$-$Rosa^{TdT}$ mice were maintained under pathogen-free conditions at Institute Gustave Roussy. Pancreatic tissue samples from genetically engineered mouse models of PDAC ($Kras^{LSL\text{-}G12D/+}$;$Tpr53^{LSL\text{-}R270H/+}$;$Pdx1^{Cre/WT}$) were kindly provided by Francesco Novelli (Department of Molecular Biotechnology and Health Sciences, University of Turin, Turin, Italy).

Orthotopic tumors. To establish orthotopic models, 6- to 9-weeks old female mice were anesthetized with isoflurane and subjected to surgical procedure. After left abdominal incision, pancreatic tails were exposed and injected with 5 x 10^5 tumor cells resuspended in cold PBS mixed at 1:4 dilution with Matrigel (Corning) in a final volume of 50µL. Mice were monitored with ultrasound imaging to measure tumor progression.

Heterotopic tumors. To establish heterotopic tumors, a total of 2 x 10^6 cancer cells were resuspended in 200uL of endotoxin-free PBS and injected subcutaneously in the right flank of mice. Tumor growth was monitored using a digital caliper. Tumor volume was estimated assuming ellipsoidal shape as $(a \bullet b)^2 \bullet \pi/6$.

***In vivo* treatments.** The COX2 inhibitor, Celecoxib, was prepared at a concentration of 2 mg/mL in a solution of 10% DMSO, 50% Poly(ethylene glycol) - Average Mn 400 (PEG400) (Sigma), and 40% Cell Culture Grade Water (Corning) and 200 µL (400µg/mouse) were administered daily through oral gavage[6]. For IL-1β neutralization, mice were intraperitoneally injected with 50µg/mouse of anti-IL-1β monoclonal antibody (Clone B122, InVivoMAb, BioXCell) or isotype control (Polyclonal Armenian Hamster IgG, InVivoMAb, BioXCell) on the day of tumor inoculation and on day 1 post inoculation (p.i.). Starting from day 4 p.i., mice were injected three times a week for the entire duration of the experiment. $CD8^+$ T cells depletion was achieved by injecting mice intraperitoneally with 300µg/mouse of anti-mouse CD8α (Clone 2.43, BioXCell) antibody or isotype control (Clone LTF-2, BioXCell) two days before tumor injection. Starting from day 4 p.i., mice were treated twice a week with 200 µg/mouse of antibody or isotype control for the entire duration of the experiment. Depletion of $CD8^+$ T cells was confirmed by FACS analysis on blood and tumor samples. NK cells depletion was achieved by injecting the mice with a combination of 200µg/mouse of anti-mouse NK1.1 (clone PK136, BioXCell) and 50µL/mouse of anti-ASIALO GM-1 (clone Poly21460, BioLegend) or isotype control (clone C1.18.4, BioXCell) one day before and one day after

tumor inoculation. Starting from day 4 p.i., mice were injected twice a week for the entire duration of the experiment. Depletion of NK cells was confirmed by FACS analysis on blood and tumor samples. For CSF-1 neutralization, mice were intraperitoneally injected with 1mg/mouse of anti-mouse CSF1 monoclonal antibody (Clone 5A1, BioXCell) or isotype control (clone HRPN, BioXCell) 3 days before tumor inoculation. Starting from day 1 p.i., mice were injected with 500µg/mouse every 5 days. Depletion of monocytes was assessed by FACS analysis on blood and tumor samples.

Bone Marrow (BM) chimeras. Recipient mice were lethally irradiated with two doses of radiations for a total of 935 cGy. The following day, irradiated mice were transplanted with 5 x 10^6 total BM cells by intravenous injections. BM chimerism was checked by measuring the percentage of CD45.1/CD45.2 cells in blood samples by flow cytometry 4- and 10-weeks post transplantation. BM chimeras were inoculated with KPC cells 12-weeks post transplantation.

Tissue processing. Human and murine PB samples were incubated with Red Blood Cell (RBC) lysis buffer (Biolegend) for 10 min on ice and washed with Phosphate Buffered Saline (PBS). Cells were centrifuged for 5 min at 450 x g and resuspended in the appropriate buffer for down-stream application. Freshly resected human PDAC samples were minced in small pieces and digested with the Tumor Dissociation kit, human (Miltenyi Biotec). Similarly, murine healthy pancreas and tumors were manually minced in small pieces and dissociated with the Tumor Dissociation kit, mouse (Miltenyi Biotec) following manufacturer's instructions. The obtained single cells suspensions were filtered on 70µm cell strainers, incubated with RBC lysis buffer for 10 min on ice and resuspended in the appropriate buffer for cell counting and down-stream application. In selected experiments, murine tumor-draining lymph nodes were smashed, filtered through a 70µm cell strainers, and resuspended in the appropriate buffer for down-stream application. For the collection of plasma samples, an aliquot of 300 µl of blood collected into EDTA tubes was centrifuged 5 min at 10,000 x g. Plasma was transferred into a clean tube

and re-centrifuged 5 min at 10,000 x g. Plasma samples were frozen and stored at −80 °C until use. Supernatants of human PDAC and normal adjacent tissues were generated by culturing weighted tissues (1 to 30mg) in 1mL of complete media in a 48 well-plate. After 48 hours, supernatants were collected, centrifuged for 5 min at 450 x g to remove cellular debris and stored at -80°C until use. For mass-spectrometry experiments, tissue samples were chopped, weighted and immediately snap-frozen at -80°C.

Culture of mouse monocytes and macrophages. Bone marrow cells were collected by crushing the hips, femurs, and tibias of female mice in 50 mL of sterile PBS, filtered through a 70µm cell strainer, and centrifuged for 5 min at 450 x g. Red blood cells were lysed using 0,2% NaCl solution, followed by 1,6% NaCl solution. BM cells were filtered through a 70µm cell strainers and centrifuged for 5 min at 450 x g. For BMDM differentiation, cells were counted and seeded in IMDM supplemented with 20% FBS, 20% L929-conditioned media containing M-CSF, antibiotics (penicillin G 100 U/ml and streptomycin sulfate 100 U/ml), 2 mM L-glutamine and 5 µM 2-mercaptoethanol. Four days after culture, fresh medium was added to the cells. At day 7 after plating, cells were stimulated as described below. Monocytes were isolated from total BM cells using the mouse Monocyte Isolation Kit (BM, Miltenyi Biotec), following manufacturer's instructions. At the end of the isolation procedure, cells were > 90-95% $CD11b^{+}Ly6G^{-}Ly6C^{+}$ as assessed by flow cytometry. Monocytes were counted and seeded in U-bottom 96 well-plates at a density of 1 x 10^5 cells/well in RPMI supplemented with 10% FBS, antibiotics (penicillin G 100 U/ml and streptomycin sulfate 100 U/ml) and 2 mM L-glutamine. One hour after plating, monocytes were stimulated as described below.

***Ex vivo* stimulation of mouse cells.** Cells were stimulated with TNF-α (10 ng/mL), PGE_2 (1µM), IL-1β (10 ng/mL). For stimulation with Tumor Conditioned Medium (TCM), KPC cells were stimulated or not for 24 hours with either IL-1β (10 ng/mL), Cox2-inhibitor SC-236 (Cayman Chemical) (10µM), or their combination. At the end of the stimulation, TCM were

collected, centrifuged for 5 min at 450 x g to remove cellular debris, filtered through 0,22µm strainer and stored at -80°C. Before BMDMs stimulation, thawed TCM were incubated at 37°C for 30 min with anti-TNF-α antibody (25µg/mL; Clone XT3.11, InVivoMAb, BioXCell) or isotype control rat IgG1 anti-horseradish peroxidase (25µg/mL; Clone HRPN, InVivoMAb, BioXCell). To rule out any carryover effect of Cox2-inhibitor, fresh SC-236 (10µM) was added to the TCM before stimulating BMDMs.

Generation and culture of mouse PDAC spheroids. For the establishment of mouse pancreatic tumor spheroid culture, 1 x 10^4 WT and COX2-KO KPC cells were resuspended in 50 µL Matrigel, plated in 4-well culture plates (Nunc) and grew in Mouse Complete Medium (Advanced DMEM/F12) supplemented with 10 mM HEPES, antibiotics (penicillin G 100 U/ml and streptomycin sulfate 100 U/ml), 1% GlutaMax, B-27 Supplement, 10 mM Nicotinamide, 1.25 mM N–Acetylcysteine, 10 ng/mL recombinant human R–Spondin1, 100 ng/mL recombinant human FGF10, 100 ng/mL recombinant human Noggin, 500nM A83–01, 50 ng/mL recombinant human EGF, 10 nM Gastrin1, and 10.5 µM Y–27632). Spheroid cultures were split at confluency by dissolving Matrigel in cold Splitting Medium (Advanced DMEM/F12 supplemented with 10mM Hepes, 1% GlutaMAX and antibiotics (penicillin G 100 U/ml and streptomycin sulfate 100 U/ml)). Spheroids were then mechanically disrupted with a 21 Gauge needle syringe, centrifuged for 5 min at 300G, and washed with Splitting Medium. After a second centrifugation, dissociated spheroids were resuspended in Matrigel and spotted as domes (50 µL/dome) in 4-well culture plates with Mouse Complete Medium. For orthotopic injections, WT and COX2-KO KPC-derived spheroids were collected after 6 passages in cold Splitting Medium and centrifuged at 300G for 5 min at 8°. Spheroids were then mechanically dissociated, centrifuged at 300G for 5 min, and resuspended in a solution of 25% Matrigel in PBS. Dissociated spheroids (1 x 10^6 cells in 50 µL) were injected orthotopically in immune-competent mice as described above.

Generation and culture of mouse PDAC organoids. Murine PDAC organoids from IL1R1 WT or IL1R1 KO KPC cells were generated according to previously published protocol[7]. Briefly, IL1R1 WT or IL1R1 KO KPC cells were subcutaneously injected into C57BL/6N mice as described above. 11 days p.i., tumors were explanted and manually minced into 1-2 mm^3 pieces in Splitting Medium, incubated for 1-2 hours at 37°C in pre-warmed Digestion Solution (Basal Medium supplemented with 0.125 mg/mL Collagenase type I, 0.125 mg/mL Dispase II and 0.1 mg/mL DNase I), and further mechanically dissociated by vigorously pipetting. Dissociated samples were then filtered through a 70 µm Cell Strainer and washed with cold Wash Medium (DMEM high glucose supplemented with 1% FBS and antibiotics (penicillin G 100 U/ml and streptomycin sulfate 100 U/ml)). Cells were pelleted at 300G for 5 min at 8 °C and washed twice with Wash Medium. Finally, tumor cells were resuspended in cold Matrigel, plated into 50 µL dome/well. After Matrigel solidification, 500µL of warm Mouse Complete Medium supplemented with 10.5 µM Rock Inhibitor were added to each well.

***In vitro* stimulation of murine PDAC organoids.**

Four domes of organoids (passage 3) obtained from either IL1R1 WT (n=4) or IL1R1 KO (n=4) tumors were incubated in Dispase solution (Splitting Medium supplemented with 2mg/mL Dispase II) for 20 min at 37°C, to allow matrix dissociation. Matrix-free organoids were centrifuged at 300 x g for 5 min at 8°C, and dissociated by incubation with TrypLE digestion enzyme at 37°C for 10 min, followed by addition of Dispase Solution supplemented with 0.1 mg/mL DNase I for 10 min. Cells were counted and seeded at 5 x 10^3 single cells/well in 4 wells of 8-Well Glass Bottom µ-Slides (Ibidi) in a final volume of 100 µL Matrigel/well. Cultures were maintained in Mouse Complete Medium supplemented with 10.5 µM Rock Inhibitor and stimulated with 10 ng/mL IL-1β where indicated, replacing the medium and the stimulus every 72 hours for a total of five days.

Analysis of organoid-forming efficiency.

For freshly prepared organoids, the forming efficiency was assessed after 6 days of culture. Each tumor (n=4/group) was plated in 8 domes, and for each dome four different brightfield images were captured to allow the counting of live organoids. Then, the mean number of organoids per field, normalized for the volume of the tumor of origin, was calculated.

For organoids stimulated with IL-1β, samples were fixed for 20 min in 4% PFA at 37°C and processed for immunofluorescence analysis. Briefly, after fixation, organoid cultures were permeabilized with PBS + 0.5% Triton X-100 at 37°C for 30 min and then incubated in blocking buffer (PBS + 5% BSA + 10% Donkey Serum (Jackson Immunoresearch) + 0.5% Triton X-100) at 37°C for 30 min. Samples were then incubated with Alexa Fluor™ 488 Phalloidin (Invitrogen A12379, 1:200) in 1% BSA for 3 hours at room temperature. Nuclei were counterstained with DAPI for 10 min at room temperature. Samples were imaged on an Olympus FluoVIEW 3000 RS confocal laser scanning system using UPLXAPO 4X/0.16 objective, by acquiring 3 x 3 grids and optical sections of 33µm each (1,95AU) were collected for each well to cover the entire Matrigel area.

Data processing. Image segmentation was performed using the Machine Learning Tool of the Arivis Vision 4D software (ZeissAG) using annotated regions of interest as training input. Identified image objects were filtered by sphericity (> 0.6) and volume (> 10^3 µm³). The volume and the number of organoids for each well were calculated and exported for statistical analyses. The same parameters for organoid identification were applied to all the imaged samples.

***In vitro* stimulation of tumor cells and organoids with IL-1β for gene expression analysis.** KC, KPC cell lines (2D) and KPC-derived organoids (3D) were cultured as described above and stimulated with IL-1β to the final concentration of 10ng/mL for the indicated time points or left untreated. At the end of the stimulation, KPC organoids were dissolved in cold Cell Recovery Solution (Gibco) at 4°C for 20 min in agitation, centrifuged at 400g for 5 min at 4°C,

and resuspended in Lysis buffer (ReliaPrep RNA Cell Miniprep System, Promega). Bulk and scRNA-Seq were performed as described below.

Lentiviral transduction of KPC cells. *Il1r1* cDNA was synthetized and cloned in the pCCLsin.PPT.hPGK.GFP.wpre plasmid by GenScript DNA Synthesis service. Lentiviral vectors (LV) were produced, concentrated and titrated as previously described[8]. For KPC transduction, single IL1R1 KO clones (2 x 10^5 cells) were transduced with a multiplicity of infection (MOI) of 10. Two weeks after transduction, IL1R1$^+$ cells were sorted (FACSAria instrument; BD Biosciences) and expanded *in vitro* for tumor inoculation. Polyclonal IL1R1-reconstituted pools were generated mixing an equal amount of 5 validated clones. The presence of the targeted protein was further validated by western-blot analyses.

Flow cytometry. If not differently stated, single cell suspensions were incubated with anti-mouse FcγIII/II receptor (CD16/CD32) blocking antibody for 10 min on ice and pelleted by centrifugation. Cell viability was assessed by Aqua Live/Dead staining, applied for 30 min at 4°C. Surface staining was then performed with fluorophore-conjugated primary antibodies for 30 min at 4°C. For intracellular staining, samples were fixed with IC Fixation Buffer (Biolegend) and permeabilized with Intracellular Staining Perm Wash Buffer 10X (Biolegend) according to manufacturer's instructions. For detection of intracellular IFN-γ and TNF-α, tumor-draining lymph nodes were processed as described above. Single cell suspensions were incubated in a 96 well-plate with Cell Activation Cocktail with Brefeldin A (Biolegend) for 3 hours at 37°C, and then stained as described above. To assess cell apoptosis and viability, KC and KPC cells (WT and COX-2 KO) were washed with cold PBS and resuspended in AnnexinV binding buffer (PE AnnexinV Apoptosis Detection kit, Biolegend). Cells were stained following manufacturer's instructions. For the quantification of the intracellular IL-1β in monocytes, total BM cells were seeded in a 48 well-plate at a density of 2 x 10^6 cells/well in IMDM supplemented with 10% FBS, antibiotics (penicillin G 100 U/mL and streptomycin

sulfate 100 U/mL) and 2 mM L-glutamine and stimulated as indicated. After stimulation, samples were processed for flow cytometry analysis as reported. After exclusion of doublets and dead cells, monocytes were gated as $CD11b^+$ $Ly6G^-$ $Ly6C^+$. Absolute cell count was performed using Precision Count Beads™ (Biolegend), following manufacturer's instructions. All samples were acquired on BD FACSymphony and FACSCanto II using DIVA software v.8.0.2 (BD Biosciences). Data were analyzed with FlowJo Software (v. 10.8.1).

Cell proliferation assay. KC or KPC cells were seeded in a 96 well-plate at a density of 1 x 10^4 cells/well in technical triplicate. After 4, 24, 48, and 72 hours of culture, 10µL/well of WST-1 reagent (Abcam) was added and cells were incubated for 30 min in standard culture conditions. After incubation, OD values (450nm) were acquired at Multiskan GO Microplate Spectrophotometer (Thermo Scientific) and proliferation was calculated as fold-change over the 4 hours.

RT-qPCR. Total RNA was extracted using the ReliaPrep RNA Cell Miniprep System (Promega) and quantified with NanoDrop 8000. Single-stranded cDNA was synthesized using ImProm-II Reverse Transcription System (Promega) starting from 400-500 ng total RNA. For monocytes isolated from total BM, cDNA was synthesized using SuperScript II (Thermo Scientific), amplified via PCR with KAPA HiFi HotStart (Roche) and purified with AMPure XP beads (Thermo Scientific). Sample concentration was assessed by Qubit 3.0 and size distribution by an Agilent 4200 Tapestation system. Amplification of target genes was performed with Fast SYBR Master Mix on a ViiA7 Real-Time PCR System. A complete list of primer pairs used is reported in the **Supplementary Table 4**.

Analyses of cell culture supernatant. Murine BMDMs, BM monocytes and tumor cells were stimulated as indicated. For quantification of IL-1β, murine BMDMs and BM monocytes were stimulated for 4hrs as indicated and ATP (5mM) was added for the last 30 min of stimulation. Supernatants were collected and centrifuged to remove cellular debris. IL-1β (Mouse IL-1 beta

Uncoated ELISA, Invitrogen) and M-CSF (DuoSet ELISA Mouse M-CSF; R&D) were measured following manufacturer's instructions. Absorbance was measured on a Multiskan GO Microplate Spectrophotometer. Other human and murine cytokines were measured using Bio-Plex Pro™ Mouse Chemokine 31-Plex Assays (Bio-Rad) and Bio-Plex Pro Human Cytokine Screening Panel, 48-Plex (Bio-Rad), according to the manufacturer's indications. Acquisition was performed using Luminex instruments and analyzed with Bio-plex manager (Bio-Rad) software.

PGE_2 levels were quantified either in the supernatants of human tissue samples, obtained as described above, or in the supernatants of KC, KPC and Panc02 cell lines. KC and KPC cells were seeded at 1 x 10^6 cells per 10 cm dish and cultured for 24-48 hours in 6 mL of complete medium. Supernatants were collected and centrifuged to remove cellular debris. PGE_2 (Prostaglandin E_2 Express ELISA kit, Cayman Chemical) was measured following manufacturer's instructions. Absorbance was measured on a Multiskan GO Microplate Spectrophotometer. When indicated, PGE_2 levels were normalized on tissue weight.

Extraction of prostaglandins (PGs) by SPE (C-18) purification. PGs were extracted as previously described (doi: 10.1194/jlr.D700030-JLR200) with minor modifications. Briefly, 35 mg of tissue was homogenized in 3 ml of 15% methanol in water at pH 3 (containing formic acid 0.04%) containing PGE_2-d4 and PGD_2-d4 (40 ng each) as internal standards and 0.005% BHT to prevent PGs oxidation, using an electric pestle. The homogenate was then vortexed for 5 min and subjected to 10 min of centrifugation (2,000 x g) at 4°C to remove the precipitated proteins. The supernatant was loaded onto an OASIS HLB prime vac Cartridge (3cc) and allowed to completely enter the packing material. The cartridge was washed with 3 ml 15% methanol and 3 ml water. The PGs were eluted from the cartridge with 3 ml ethyl acetate containing 1% methanol. The eluted samples were dried under nitrogen and resuspended with 50 µl acetonitrile/water (1:2) and stored at -20 °C until LC-MS/MS analysis. For PGE_2 and

PGD_2 absolute quantification, calibration curves were prepared by spiking increasing amount of PGA1 (from 0.0625 ng to 625 ng) in the same sample matrix (murine or human control sample). The calibration curve point samples were then processed as described above, including the addition of PGE_2-d4 and PGD_2-d4 (40 ng each) for the extraction yield correction.

Chromatographic separation of PGE_2 and PGD_2 and their LC-MS/MS detection. Samples were directly analysed using the UPLC 1290 (Agilent Technologies) coupled to the TripleTOF 5600+ mass spectrometer (SCIEX) (ProMeFa, Proteomics and Metabolomics Facility, Ospedale San Raffaele, Milan, Italy). Chromatographic separations occurred on C18 column (ACQUITY UPLC HSS T3 Column, Waters, 1.8 µm, 2.1 mm x 100 mm) by directly injecting 10 µl of samples (1/5 of the original sample). Metabolites were separated using a flow rate set at 0.4 ml/min and a gradient of solvent A (water, 0.1% formic acid) and solvent B (acetonitrile, 0.1% formic acid). The gradient, in negative mode, started from 25% B hold for 2 min; increased up to 40 % B in 16 min; increased again up to 90% in 1 min; maintained constant at 90% B for 4 min; decreased to 25% B in 1 min and maintained at 25% for 2 min. The column was set at 50°C while the samples were kept at 4°C. Full scan spectra were acquired in the mass range from *m*/*z* 50 to 500. Automated calibration was performed using an external calibrant delivery system (CDS) which infuses APCI negative calibration solution every 5 samples injection. A product ion experiment mode was used to monitor PGE_2 and PGD_2 mass (at 351.2 m/z) as well as internal standards PGE_2-d4 and PGD_2-d4 (355.4 m/z). PGA1 at 335.4 m/z was followed for the calibration curves. The source parameters were: Gas 1: 33 psi, Gas 2: 58 psi, Curtain gas: 25 psi, Temperature: 500 °C and ISVF (IonSpray Voltage Floating): -4500 V, DP: -80 V, CE: 44 V.

Immunofluorescence staining. For immunofluorescence analysis of macrophage spatial distribution, tissues were fixed overnight in 4% paraformaldehyde at 4°C, washed in PBS and

placed in 30% sucrose for 12-24 hours. Afterwards, tissues were placed in a 2:1 mixture of 30% sucrose and optical cutting temperature (OCT) compound (Bio Optica, 05-9801) for 30 min at 4°C, embedded in OCT and snap frozen in dry ice. 10-µm cryostat sections were fixed in paraformaldehyde (4% in PBS) at room temperature for 20 min, washed three times in 0.05% PBS-Tween (PBS-T) and incubated with blocking buffer (0.05% PBS-T + 0.3% Triton X-100 + 5% BSA) at room temperature for 1 hour. Sections were stained overnight at 4°C with the following primary antibodies: rat anti-mouse F4/80 (Abcam ab6640, 1:200) or rabbit anti-mouse F4/80 (Abcam ab30042, 1:500), goat anti-mouse IL-1β (R&D Systems AF-401-NA, 1:100), rat anti-mouse FOLR2 (BioLegend 153302, 1:100), rabbit anti-mouse KRT19 (Abcam ab52625, 1:500), goat anti-mouse CD31 (R&D Systems AF3628, 1:500), rat anti-mouse VEGFR2 (BD Pharmingen 550549, 1:100), rabbit anti-mouse PDGFRα (Abcam ab203491, 1:500). Sections were washed three times in 0.05% PBS-T, and incubated with the following secondary antibodies: donkey anti-rat IgG Alexa Fluor Plus 488 (Invitrogen A48269, 1:500), donkey anti-goat IgG Alexa Fluor Plus 555 (Invitrogen A32816, 1:500), donkey anti-rabbit IgG Alexa Fluor Plus 647 (Invitrogen A32795, 1:500). After three washes in 0.05% PBS-T, cell nuclei were stained with DAPI (Sigma-Aldrich Merck, MBD0015) at room temperature for 15 min and coverslips were mounted onto slides with FluorSave Reagent (Sigma-Aldrich Merck, 345789). Digital images were acquired on a MAVIG RS-G4 scanning confocal microscope (Caliber I.D.) using a 20x air objective or a 40x oil objective.

Immunofluorescence analysis of macrophage spatial distribution. Quantitative analysis of immunofluorescence images was performed using QuPath v0.4.1 (Bankhead et al. 2017). For each image, tissue-specific expression of cytokeratin 19 (KRT19) was used to annotate tumor areas and discriminate them from the adjacent stroma. Equally sized regions of interest (ROIs) were randomly selected within the annotated "tumor" ($DAPI^+$ $KRT19^+$) or "stromal" ($DAPI^+$ $KRT19^-$) areas. Within each ROI, cell segmentation was performed using the "Cell detection"

command based on the nuclear DAPI stain and thresholds were applied on fluorescence signals to create classifiers for cell type identification. Specifically, F4/80 signal was used to classify cells as macrophages and compute their abundance in annotated ROIs. Similarly, the macrophage classifier was combined with classifiers based on IL-1β and FOLR2 signals to detect double-positive cells. Quantification was performed by computing the frequency of F4/80$^+$, F4/80$^+$ IL-1β$^+$ and F4/80$^+$ FOLR2$^+$ cells in n = 10-20 ROIs per tissue section, equally distributed between tumor and stromal compartments. Additionally, the frequency of macrophages was quantified in normal adjacent tissue (NAT) from orthotopic PDAC mice and in healthy pancreas from wild-type controls. For distance analysis, the frequency of F4/80$^+$ IL-1β$^+$ and F4/80$^+$ FOLR2$^+$ macrophages was calculated within concentric partitioning rings annotated around the tumor margin (identified by KRT19 staining), with a cumulative 50-µm expansion in the adjacent stroma. The same parameters for segmentation and cell type classification were applied to all samples from the same experiment.

Immunofluorescence analysis of IL-1β$^+$ TAMs in areas of angiogenesis. Quantitative analysis of IL-1β$^+$ TAMs in areas of angiogenesis was carried out with QuPath v0.4.1 (Bankhead et al. 2017). Cell segmentation was performed on whole-tissue sections (comprising tumor and stroma) using the "Cell detection" command based on the nuclear DAPI stain and object classifiers were set up to detect CD31$^+$ VEGFR2$^+$ endothelial cells. The "Density map" command was then used to split the tissue section into areas with "high" and "low" density of CD31$^+$ VEGFR2$^+$ endothelial cells, and quantify the frequency of F4/80$^+$ IL-1β$^+$ cells within these discrete tissue annotations.

Immunofluorescence analysis of IL-1β$^+$ TAMs in areas of hypoxia. Tumor hypoxia was labelled *in vivo* with Hypoxyprobe, following the manufacturer's instructions. Briefly, pimonidazole (Hypoxyprobe-1, 60 mg/kg of body weight) was intraperitoneally injected in end stage orthotopic KPC-bearing mice 60 min before euthanasia. Fresh tumor biopsies were

351 washed in PBS, embedded in OCT compound and snap frozen in dry ice. 10-µm cryostat
352 sections were processed for immunofluorescence staining as described above, using the
353 following primary antibodies: rat anti-mouse F4/80 (Abcam ab6640, 1:200), rabbit anti-mouse
354 KRT19 (Abcam ab52625, 1:500), goat anti-mouse IL-1β (R&D Systems AF-401-NA, 1:100),
355 anti-pimonidazole (Hypoxyprobe PAb2627AP, 1:20). Digital images were acquired on a
356 MAVIG RS-G4 scanning confocal microscope (Caliber I.D.) using a 20x air objective.
357 Quantitative analysis was carried out with QuPath v0.4.1 (Bankhead et al. 2017), by
358 performing DAPI-based cell segmentation of the whole tumor and stroma and using the
359 "Density map" command to define annotations comprising areas with high density of cells
360 stained for Hypoxyprobe. The ensuing density maps were then used to annotate tissue regions
361 as "hypoxic" or "non hypoxic" and quantify the frequency of $F4/80^+$ $IL\text{-}1\beta^+$ cells within these
362 compartments.
363 **Immunohistochemistry (IHC) staining of human PDAC.** Immunohistochemistry staining
364 of human PDAC tissue was performed using the DISCOVERY ULTRA (Roche/Ventana)
365 platform. Briefly, 5-µm tissue sections collected from FFPE blocks of human PDAC were
366 deparaffinized, subjected to antigen retrieval with DISCOVERY CC1 solution
367 (Roche/Ventana, 950-500) for 60 min and blocked with DISCOVERY Inhibitor
368 (Roche/Ventana, 760-4840) for 8 min. Tissue sections were sequentially stained for 30 min at
369 RT with the following primary antibodies: rabbit anti-human NLRP3 (Sigma-Aldrich Merck
370 HPA012878; 1:150), mouse anti-human CD163 (MRQ-26, Cell Marque 163M-18, pre-
371 diluted), mouse anti-human FOLR2 (Invitrogen MA5-26933, 1:100), mouse anti-human
372 cytokeratin 8 & 18 (B22.1 & B23.1, Cell Marque 818M-90, pre-diluted). For each staining
373 cycle, incubation with primary antibody was followed by incubation with DISCOVERY
374 UltraMap anti-Ms HRP (Roche/Ventana, 760-4313) or DISCOVERY UltraMap anti-Rb HRP
375 (Roche/Ventana, 760-4315) for 20 min at RT, and then with one of the following fluorophores

at 1:100 dilution for 4-8 min at RT: DISCOVERY FITC kit (Roche/Ventana, 760-232), DISCOVERY Red 610 kit (Roche/Ventana, 760-245), DISCOVERY Cy5 (Roche/Ventana, 760-238). Tissue sections were neutralized with DISCOVERY Inhibitor at the end of each staining cycle to avoid cross-reactivity. Finally, tissue sections were counterstained with DAPI and coverslips were mounted onto slides using VECTASHIELD Antifade Mounting Medium (Vector Laboratories, H-1000-10). Digital images were acquired on a MAVIG RS-G4 scanning confocal microscope (Caliber I.D.) using a 20x air objective.

Western Blot analyses. Cells were lysed in a radioimmunoprecipitation assay (RIPA) lysis buffer, containing 10 mM Tris-HCl pH 8, 1 mM EDTA pH 8, 140 mM NaCl, 1% Triton X-100, 0.1% SDS, 0.1% deoxycholate and protease/phosphatase inhibitors. Protein concentrations were measured with the Pierce™ BCA Protein Assay Kit. Lysates were then electrophoresed on Tris-glycine sodium dodecyl sulfate/polyacrylamide gel electrophoresis (SDS/PAGE) gels and transferred on Nitrocellulose membranes (Amersham™ Protran™ Premium 0.45 µm NC). Membranes were blocked in PBS-T buffer added with 5% BSA or 5% Milk (1 hour at room temperature), followed by overnight incubation with primary antibodies at 4°C: anti-IκBα (#9242S, Cell signaling, 1:1000), anti-IL1R1 (ab229051, Abcam, 1:1000) and anti-COX2 (160106, Cayman Chemical, 1:100). The following day, membranes were washed and incubated for 1 hour at room temperature with HRP-conjugated secondary antibody. Membranes were developed either with Clarity™ Western ECL Substrate (BIO-RAD) or Westar Supernova (CYANAGEN). Protein loading was assessed by detecting anti-β-actin (A1978, Sigma-Aldrich, 1:2000) or anti-Vinculin (#13901S, Cell Signaling, 1:1000).

Generation of and processing of single-cell RNA-Seq data

Data generation. Human and murine samples were collected and dissociated as described above. For the patient LiMeT PDAC15, cells were enriched in the myeloid fraction as $CD45^{+}CD3^{-}CD19^{-}$ by sorting (FACSAria, BD Biosciences). For heterotopic and orthotopic

KC tumors, cells were enriched in the myeloid fraction as $CD45^{+}Cd11b^{+}$ via sorting and scRNA-Seq libraries generated using the Chromium Single Cell 3' Reagent Kit v2, according to the manufacturers' instructions. For murine KPC organoids, Matrigel domes containing the organoids were dissolved in Cell Recovery Solution (Gibco) for 30 min on ice, manually inverting the tubes every 5 min. After addition of cold basal medium, organoid suspension was centrifuged and supernatant was removed prior to incubation in TrypLE Express (Gibco) for 20 min on an orbital shaker at 37°C. The larger cellular aggregates were allowed to settle by gravity, and the single cell suspension was collected from the supernatant without interfering with the lower fraction. Upon centrifugation at 400 g for 5 min at 4°C, cells were resuspended in ultrapure BSA (400ug/mL) (Invitrogen) for downstream processing.

If not differently stated, scRNA-Seq libraries were generated using a microfluidics-based approach on Chromium Single-Cell Controller (10X Genomics) using the Chromium Single Cell 3′ Reagent Kit v3.1, according to the manufacturers' instructions. Briefly, single cells were partitioned in Gel Beads in Emulsion (GEMs) and lysed, followed by RNA barcoding, reverse transcription and PCR amplification (13-15 cycles). The concentration of the scRNA-seq libraries was determined using Qubit 3.0 and size distribution was assessed using an Agilent 4200 TapeStation system. Libraries were sequenced on an Illumina NovaSeq 6000 instrument (paired-end, 150bp read length).

Data processing. Fastq files were processed with Cell Ranger (v 4.0.0)[9], using default parameters. Reads were aligned to reference genome mm10 for mouse samples and hg38 for human samples (references version 2020-A, 10X Genomics). Only confidently mapped reads with valid barcodes and unique molecular identifiers (UMIs) were retained to compute a gene expression matrix containing the number of UMI for every cell and gene. Gene counts were imported in R environment (v 4.0.3) and processed with Seurat (v 4.0.3). When creating the Seurat object, genes expressed in less than 3 cells were removed. Putative doublets were

identified and discarded using scDblFinder R package (v 1.4.0) [10] by imputing doublet rates (dbr) equal to 0.07 for mouse sample and 0.05 for human samples. Dbr were established in agreement with the number of loaded cells and following the 10X Genomics guidelines. Cells expressing less than 1000 UMI counts were discarded. Cells expressing less than 200 genes (mouse sample), or less than 500 genes (human sample) were also excluded. Lastly, cells with a ratio of mitochondrial versus endogenous genes expression exceeding 0.25 (mouse sample) or 0.40 (human sample) were discarded. Raw expression data were normalized applying $\log_2$ transformation with NormalizeData function, scaled using ScaleData function, regressing on percentage of mitochondrial gene expression and cell cycle scores, previously computed using CellCycleScoring function. Top 3,000 genes with the highest standardized variance were computed using FindVariableFeatures function (selection.method = "vst"). Principal component analysis (PCA) was computed using RunPCA function with default parameters.

Batch correction. PCA embeddings were corrected for sample batch by applying alternative algorithms to the same Seurat object through the Seurat Wrapper package (v 0.3.0). For both human and mouse data, when analyzing the whole or tumor cells dataset, batch effect was corrected employing matching mutual nearest neighbor (MNN) algorithm [11], implemented by RunFastMNN function using default parameters. For the analysis of mononuclear-phagocytes and tumor-associated macrophages, batch correction was achieved with the Harmony algorithm (v 0.1.0) [12], implemented by RunHarmony function using the first 30 PCA dimensions and default theta (theta=3 for human dataset).

Graph-based clustering and differential gene expression analyses. Shared Nearest Neighbor (SNN) graph was computed using the FindNeighbors function, taking as input the first 20 PCA dimensions. Cell clusters were defined using Louvain algorithm with the FindCluster function. For visualization in 2 dimensions uniform manifold approximation and projection (UMAP) [13]

was used. Cluster-specific genes were identified using FindAllMarkers function with option only.pos = TRUE and min.pct=0.1, setting a cut-off of FDR < 0.01.

Inference of copy-number variants (CNV). Single-cell CNVs were inferred using CopyKAT R package (v 1.0.5) [14]. CopyKAT estimates the genome copy number profile of single cells employing an integrative Bayesian segmentation approach combined with hierarchical clustering to identify putative aneuploid cells. CopyKAT was run separately on each human sample, taking the raw count matrix of all cells as input and adjusting the segmentation parameter KS.cut to either 0.1 or 0.15 according to data quality.

Human-mouse comparison of TAM clusters. We performed a pre-ranked GSEA analysis with clusterProfiler R package (v 3.18.1) [15] on mouse TAM genes ranked by log_2FC (each TAM subset vs other TAMs) using as gene sets mouse orthologs of human TAMs marker genes obtained using biomaRt (v 2.46.3) [16] database. To identify shared signatures for each human and mouse TAM cluster, we computed overlaps between marker genes identified using logfc.threshold = 0.8.

RNA Velocity and single-cell trajectories. Mouse classical monocytes and tumor-associated macrophages from pancreatic and blood samples were analyzed together as previously described. Batch effect correction was performed by matching mutual nearest neighbor (MNN) algorithm [11], using the RunFastMNN function with default parameters. The first 20 MNN-corrected principal components were used to compute the two-dimensional embedding using the diffusion map-based algorithm Palantir [17], implemented with the RunPalantirDiffusionMap function from SeuratExtend R package (v 0.4.2). Cell clusters were defined according to marker-based manual annotation previously done on each dataset. The Seurat object was then converted into Scanpy format (v 1.6.0) [18] using SeuratDisk (v 0.0.0.9019) and the following analyses were performed in Python environment (v 3.6.10). To annotate spliced and unspliced reads, cell-barcode sorted bam files from Cell Ranger output were processed using Velocyto

pipeline (v 0.17.17) [19]. The scVelo Python package (v 0.2.2) [20] was used to compute RNA velocity vectors for each gene, employing dynamical modeling to estimate splicing kinetics. Using CellRank package (v 1.2.0) [21], RNA velocity and transcriptomic similarity information were combined in single kernel to compute a cell-cell transition matrix. Generalized Perron Cluster Cluster Analysis (GPCCA) estimator [22] was used to identify macrostates. Terminal states were inferred by inspecting the coarse-grained transition matrix and were then used to compute absorption probabilities. Focusing on the Classical Monocyte - *Il1b*$^{+}$ TAMs lineage, genes whose expression correlates with absorption probabilities towards Il1b+ TAMs terminal state were identified as potential lineage drivers.

Optimal transport analysis. To infer cell trajectories, we applied Waddington optimal transport [23] on our scRNA-Seq mouse time-course data. Optimal transport model was fit to classical monocytes and tumor-associated macrophages from pancreatic and blood samples, setting ε=0.05, λ1=1 and λ2=50 to compute transport maps. Based on them, we computed cell fate probabilities using cell populations at day30 as endpoint.

Gene set enrichment analysis (GSEA). Hallmarks gene sets were retrieved from msigdbr (v 7.5.1)[24]. For Gene Ontology biological processes gene sets, we used org.Hs.eg.db (v 3.12.0) and org.Mm.eg.db (v 3.12.0) as genome wide annotations for human and mouse respectively. Gene sets of cytokine-induced signatures were derived from *in vitro* stimulation experiments on mouse bone marrow-derived macrophages[25,26] (Supplementary Table 4).

IL1B gene expression in human cell types. To evaluate the expression of *IL1B* across all human cell types, we reanalyzed scRNA-Seq data including neutrophils in the dataset. Neutrophils were retrieved lowering the cutoffs on UMI counts and genes per cell to 500 and 100, respectively. Data were processed as previously described, with the exception that counts were normalized with SCTransform function in Seurat.

Reanalysis of human PDAC cells in Naïve samples. Tumor cells from untreated patients were analyzed separately as previously described. We computed new embedding and clustering on cells showing variable expression of the T1RS signature (clusters 1,3,5 at resolution 0.3) and then we performed trajectory analysis with slingshot[27] (v. 1.8.0) on the MNN space. We correlated gene expression with pseudotime, computed with slingPseudotime function. To evaluate if cell trajectory reflected the acquisition of the expression of T1RS signature we performed GSEA analyses on gene list ranked by correlation values. Finally, to define which ligand-receptor interaction in the crosstalk between IL1B+ TAMs and Tumor cells drives the acquisition of the T1RS gene expression pattern through the trajectory, we performed a cell-cell communication analysis with NicheNet[28] (v. 1.1.1). We interrogated NicheNet database using IL1B+ TAMs as sender cells and Tumor cells as receiver cells. Putative ligands were selected filtering for genes expressed in IL1B+ TAMs subset (percentage of cells > 15% and $\log_2$FC[IL1B+ TAMs/Other TAMs] > 0.5), while putative receptors were selected filtering for genes expressed in the tumor cells (percentage of cells > 15% in clusters 1,3,5). We used markers of the cluster at the endpoint of the trajectory ($\log_2$FC > 1 and min.pct=30%) as target genes for ligand prioritization.

scRNA-Seq datasets collected in this study. We collected published scRNA-seq data on human pancreatic ductal adenocarcinoma and normal adjacent tissue (CRA001160)[29]; immune cells from idiopathic or hereditary pancreatitis and normal pancreas (GSE165045)[30]; pancreatic epithelial cells from GEMMs of PDAC progression (GSE207943)[31]. For these datasets we downloaded: raw fastqs, raw count matrices and normalized counts, respectively. In addition, we collected published scRNA-seq data on human hepatocellular carcinoma (GSE156625) [32], lung adenocarcinoma (GSE131907) [33], glioblastoma [34], colorectal cancer (GSE132465) [35], breast (GSE114725) [36] and renal cancer [37]. For these datasets we downloaded raw count matrices and processed them as described above.

scRNA-Seq dataset from pancreatitis patients. Raw counts matrices of immune cells from idiopathic or hereditary pancreatitis and normal pancreata were filtered to discard cells expressing less than 200 genes, less than 1000 UMIs and with a ratio of mitochondrial versus endogenous genes expression exceeding 0.20. Cells were processed as previously described, using 2000 variable features. For the analysis of macrophages, anchoring-based transfer learning[38] was used to perform annotation, using our tumor-associated macrophage dataset as reference. Anchors for transfer learning were computed using the FindTransferAnchors Seurat function. Reference labels were then projected onto query macrophages using the TransferData function. Macrophages from pancreatitis and donor pancreata were annotated according to our reference classification if the prediction score exceeded 0.75, otherwise were left unlabeled.

scRNA-Seq datasets from other mouse models. scRNA-Seq datasets from GEMM mouse models and WT and COX-2 KO KPC were processed as previously described. For scRNA-Seq data derived from heterotopic and orthotopic KC tumors we corrected batch effect employing Harmony algorithm (v 0.1.0) [12], implemented by RunHarmony function using the first 30 PCA dimensions and theta=1. For the reclustering of mononuclear-phagocytes, batch correction was achieved with the Harmony algorithm (v 0.1.0) on the first 30 PCA dimensions and default theta. Differentially expressed genes in the comparison between cells from WT and COX-2 KO tumors were computed using FindAllMarkers function with option only.pos = FALSE, min.pct=0.1, setting a cut-off of FDR < 0.01 and average $\log_2$FC>0.5.

Generation and processing of spatial transcriptomic (ST) data

Visium Spatial Gene Expression

Data generation. Spatial transcriptomics data were generated using the Visium Spatial Gene Expression Reagent Kits (10X Genomics) according to the manufacturer's instruction. Tumor biopsies from day-30 orthotopic PDAC mice were gently washed in PBS, snap frozen via bathing in liquid nitrogen-chilled isopentane and embedded in OCT compound. From 5 to 10

549 sections were collected to evaluate RNA quality at TapeStation system (Agilent). The tissue
550 blocks were then processed to retrieve 2 non-sequential 10µm sections (100 µm apart), which
551 were placed within the 6.5x6.5 mm capture areas of a Visium slide equilibrated at cryostat
552 temperature (-20°C). Sections were immediately fixed in chilled methanol at -20°C for 30 min
553 and stained via immunofluorescence using buffers supplemented with Recombinant RNase
554 inhibitor (Takara 2313A, 2 U/µl) to prevent RNA degradation. Whole-slide images were
555 acquired using the MAVIG RS-G4 (Caliber I.D.) confocal microscope at 20x magnification.
556 Barcoded libraries were generated by permeabilizing tissue sections at 37°C for 15 min and
557 performing *in situ* reverse transcription at 53°C for 45 min, followed by second-strand
558 synthesis at 65°C for 15 min. cDNA was denatured and transferred to tubes for PCR
559 amplification and library construction, including fragmentation, adaptor ligation and sample
560 indexing. The quality of both amplified cDNA and final libraries was determined at
561 TapeStation system (Agilent). Visium libraries were sequenced on an Illumina NovaSeq 6000
562 instrument (paired-end, 150bp read length).
563 ***Data processing.*** ST data were aligned to their corresponding IF image, using SpaceRanger
564 (version 1.2.0) with default parameters. We excluded spots with a number of UMI lower than
565 100 and without DAPI staining in the corresponding overlaid image, resulting in a dataset of
566 3,274 and 3,496 spots for A1 and B1 sections, respectively. To infer cell type proportions
567 within each spot, we performed cell type deconvolution using DestVI (version 0.1) [39]. We first
568 trained the single-cell latent variable model (scLVM) on the scRNA-Seq dataset obtained by
569 retaining transcriptomic data from samples collected 30 days post-tumor inoculation, analyzed
570 and annotated as described previously. We then trained the spatial transcriptomic latent
571 variable model (stLVM) on the ST dataset and we computed cell type proportions for each spot
572 with get_proportions() function. To assess spatial variability of macrophage transcriptome, ST
573 spots enriched in monocytes and macrophages were selected using the default secondary cut-

off, set by DestVI on their proportion distributions, obtaining a dataset of 671 spots for A1 and 1119 spots for B1. We computed the gamma latent space with get_gamma() function, obtaining 5 gamma values, and the Spatial Principal Components (Spatial PCs) using the get_spatial_components() function. Finally, gene expression values were imputed using get_scale_for_ct() function, extracting six different gene expression matrices from the negative binomial distribution, as predicted by the trained scLVM applied to ST latent space. The mean gene expression values computed on these expression matrices were used for downstream analysis. Spot enrichments for specific gene sets were evaluated using runPAGEEnrich() function from Giotto R package (v 1.1.2) [40]. For A1 ST dataset, we performed clustering analysis with Seurat package: spot read counts were normalized with SCTransform() function and PCA performed with RunPCA() function. Top 20 PCs were used to obtain clusters at 0.3 resolution using FindNeighbors() and FindClusters() functions. Marker genes of spots belonging to cluster 4 or cluster 6 were ranked by log_2FC and used to perform GSEA analysis for selected GO Biological Processes.

Annotation of ST spots. Single-channel grayscale IF images for sections A1 and B1 were imported in CellProfiler (v. 4.1.3) [41], rescaled using RescaleIntensity() function, and imported as composite images in Squidpy (version 1.2.3) [42]. DAPI-based cell nuclei detection was carried-out with Stardist (version 0.8.3)using the pre-trained 2D versatile algorithm for fluorescence data, to create mask binary files. In parallel, single-channel image crops were generated for every ST spot. Resulting images and masks were exported to Cell Profiler, where nuclei were filtered based on size and cell boundaries were reconstructed using the *Distance* option. A median filter was applied to F4/80, PDGFRa and KRT19 signal intensity to classify cells as positive or negative for each individual marker. Results were exported to R, double- and triple- positive cells were filtered out, and the fraction of single $F4/80^+$, $PDGFRa^+$ or $KRT19^+$ cells was calculated for all the spots. Finally, ST spots were

599 annotated as “tumor” or “stroma”, according to transcript or protein expression obtained from
600 ST or IF data, respectively. For IF-based annotation, the percentage of $KRT19^+$ cells as
601 calculated by CellProfiler was used to classify spots as tumor ($\%KRT19^+ \geq 60\%$) or stroma
602 ($\%KRT19^+ < 60\%$). For ST-based annotation, DestVI deconvolution output was used to define
603 tumor spots as those where the sum of percentages of cancer, ductal and acinar cells was ≥
604 60%. Similarly, stromal spots were defined as those where the sum of endothelial cells and
605 cancer-associated fibroblasts was ≥ 40%. Spots that did not fall in these two categories, were
606 annotated as tumor or stroma according to the most enriched cell type.

607 ***Molecular Cartography™ data***

608 ***Data generation***. 10-µm sections were collected from fresh frozen PDAC tissues, placed
609 within the capture areas of cold slides, and sent to Resolve Biosciences on dry ice for sample
610 processing. Upon arrival, tissue sections were thawed, fixed with 4% Formaldehyde (Sigma-
611 Aldrich F8775) in PBS for 20 min at 4 °C, and used for Molecular Cartography™ (100-plex
612 combinatorial single molecule fluorescence in-situ hybridization) according to the
613 manufacturer’s instructions (protocol 1.3; available for download from Resolve’s website for
614 registered users). Briefly, tissue sections were hybridized at 37°C for 24 hours with
615 oligonucleotides probes specific for the selected target genes (see Supplementary Table 9).
616 Probes were designed using Resolve’s proprietary algorithm, as previously reported[43].
617 Afterwards, probe binding was revealed with fluorescent tags in a multi-step automated
618 imaging process, repeating color development, imaging and decolorization for a total of 8
619 cycles on a Zeiss Celldiscoverer 7 instrument, using a 50x water immersion objective. The
620 resulting raw data images were preprocessed for background correction, aligned to perform
621 spot segmentation, analyzed to decode the resulting signals and to finally assign each detected
622 transcript to a *x*-*y*-*z* coordinates, as previously reported[43].

Cell segmentation. We segmented cell nuclei in the DAPI image with Cellpose[44] (v. 2.2) using the pre-trained nuclei model, with automated estimation of diameter parameter. Subsequently, cells were segmented on transcript coordinates with Baysor[45] (v. 0.5.0) using DAPI segments as prior with the following parameters: --n-clusters 1 --prior-segmentation-confidence 0.2 -m 3. Finally, we computed cells outlines by applying the convex hull algorithm, using chull R function, on transcripts assigned to each individual cell by Baysor.

Cell filtering and annotation. We imported Baysor output files and segmentation into a Seurat object with a custom function. Cells expressing less than 4 genes or more then 25 genes, along with cells with less than 10 transcripts were discarded. Gene counts were normalized with SCTransform Seurat function with clip.range set form -10 to 10. Then, we performed PCA and we computed clustering and dimensionality reduction as previously described for scRNA-Seq data. Finally, we computed markers for all cluster and annotated cell types.

Spatial neighborhood analysis. For each cluster we defined a set of cells in its spatial neighborhood, then we computed which clusters were significatively overrepresented in this neighborhood set. Briefly, for each cell we computed k-nearest neighbors within spatial coordinates space using kNN function from dbscan R package (doi:10.18637/jss.v091.i01, v. 1.1-11), with k set to 40 and maximum distance set to 400 pixels. We selected the set of nearest neighbors of all cells belonging to the same cluster and we counted the number of cells from all different cluster within this set of nearest neighbors. We then computed significance using randomly annotated data as null distribution. Specifically, we reannotated cells randomly 1000 times, maintaining cluster dimensionality and, for each randomization, we computed again the number of cells from all clusters in the set of nearest neighbors of each cluster.

Gene expression spatial correlation. We computed gene expression spatial correlation of all genes with CXCL1. First, we computed the spatial lag expression vector of CXCL1[46]. Lag expression vector of a gene reports for each cell the summed expression of its k-nearest

neighbors. Briefly, we used lag.listw from spded R package (v. 1.2-8) to compute the spatial lag vector for CXCL1, considering for each cell its 20 nearest neighbors, with maximum distance set to 400 pixels, defined with kNN function. We then correlated the real expression of each gene with the spatial lag vector of CXCL1. Genes that show high spatial correlation with CXCL1 are those genes that are more expressed in cells that are close to cells expressing CXCL1 at highest level.

ST datasets collected in this study. We downloaded raw count matrices of published GeoMX data[47] (GSE226829). We performed normalization with voom function of limma R package[48] (v. 3.46.0).

Generation and processing of bulk RNA-Seq data

Data generation. Total RNA was purified using the ReliaPrep RNA Cell Miniprep System and RNA-Seq libraries were generated using the Smart-seq2 method [49] with minor modification. Briefly, five ng of RNA were retrotranscribed, cDNA was PCR-amplified (15 cycles) and purified with AMPure XP beads. After purification, the concentration was determined using Qubit 3.0 and size distribution was assessed using Agilent 4200 TapeStation system. Then, the tagmentation reaction was performed starting from 0.5 ng of cDNA for 30 min at 55°C and the enrichment PCR was carried out using 12 cycles. Libraries were then purified with AMPure XP beads, quantified using Qubit 3.0, assessed for fragment size distribution on an Agilent 4200 TapeStation system. Sequencing was performed on an Illumina NovaSeq6000 (single-end, 75bp read length) following manufacturer's instruction.

Data processing. Reads were aligned to the mm10 reference genome using STAR aligner (v STAR_2.5.3a) [50]. Read counts matrices were computed using the featureCounts function from Rsubread package (v 2.0.1) [51], using RefSeq *Mus musculus* transcriptome (mm10) annotation [52], setting minMQS option to 255. Further analyses were performed in R environment (v 3.6.3) with edgeR R package (v 3.28.1) [53]. Expressed genes read counts were normalized using the

673 calcNormFactors function, with the Trimmed Mean of M-values (TMM) method [54]. The
674 estimateDisp function was used to estimate dispersion. Differential gene expression across
675 conditions was computed by fitting a negative binomial generalized linear model, with the
676 glmQLFit function, followed by a quasi-likelihood (QL) F-test, with the glmQLFTest function,
677 including sample replicates as covariates in the design matrix. Reads per kilo base per million
678 (RPKM) values were computed for each gene with the rpkm function.
679 ***Definition of TNF-α+PGE$_2$ synergized genes.*** RNA-Seq data were generated and pre-
680 processed as described above. Genes not passing the expression cut-off of RPKM > 1 in at least
681 two samples in the dataset were filtered out. For each timepoint we defined TNF-α-PGE$_2$-
682 inducible genes comparing expression levels in the TNF-α+PGE$_2$ condition versus UT, PGE$_2$
683 alone or TNF-α alone conditions, setting $\log_2$FC(RPKM) ≥ 1.5 and FDR < 0.01 as cut-offs.
684 We also filtered out genes not reaching RPKM > 1.5 in at least two samples within each
685 comparison. Finally, for each timepoint, we defined PGE$_2$-TNF-α synergized genes selecting
686 genes passing previously defined cut-offs in all tested comparisons. For GSEA analysis we
687 considered genes defined as PGE$_2$-TNF-α synergized in at least one timepoint.
688 ***Definition of tumor-intrinsic IL- 1β response signature (T1RS) gene signature.*** We analyzed
689 bulk and single-cell RNA-seq data on KC, KPC cells and KPC organoids stimulated with IL-
690 1β *in vitro*. For each timepoint of stimulation, we defined IL-1β -inducible genes comparing
691 expression levels in the IL-1β condition versus UT, setting $\log_2$FC(RPKM) ≥ 1 and FDR <
692 0.05 as cut-offs. For each experimental condition we defined lists of IL-1β-inducible genes,
693 selecting genes passing the defined cut-offs in at least one timepoint. Intersection of these gene
694 lists led us to the identification of a set of genes commonly induced by IL-1β in all experimental
695 conditions, namely the T1RS signature.
696 ***RNA-Seq datasets collected in this study.*** We collected published RNA-Seq data on pancreatic
697 epithelial cells from *Kras*-wild type and mutant *Kras* mice treated either with Caerulein or IL-

33 or left untreated (GSE132326, GSE154543)[55]; mouse pancreatic spheroids derived from pancreas either pre-exposed or not exposed to inflammation (GSE180211)[55]. For these datasets raw count matrices were downloaded and analyzed as previously described. In addition, we collected published RNA-Seq data of monocytes isolated from peripheral blood of PDAC patients and healthy donors (E-MTAB-11190)[56]. For these data, fastq files were downloaded and processed as previously described, using hg38 as reference genome (reference version 2020-A, 10X Genomics).

TCGA data analyses. Using the TCGAbiolinks R package (v 2.23.2) [57], we downloaded transcriptomic data and clinical data from the following cohorts: PAAD for pancreatic cancer (n=178), LUAD for lung cancer (n=517), GBM for glioblastoma (n=169), COAD for colon cancer (n=286), KIRC for renal cancer (n=533), BRCA for breast cancer (n=1095) and LIHC for liver cancer (n=374). Survival analysis on primary tumor samples was performed using the survival (v 3.2-10) and survminer (v 0.4.9) R packages.

Survival analysis of TAM markers and T1RS genes in PAAD cohort. To evaluate the prognostic significance of TAM marker genes, we obtained TAM cluster-specific genes by performing differential gene expression analysis (each TAM cluster vs other TAM clusters) and filtering for $\log_2FC \geq 1$. On such gene lists, we evaluated MNP-specificity by differential gene expression analysis, selecting genes with $\log_2FC \geq 2$ in MNP compared to other cell types identified in our scRNA-Seq data. Impact on patient prognosis was assessed by Cox beta regression coefficient on genes for which the fit was significant according to Wald test p-values corrected for multiple testing. Univariate Cox regression model was fit for the expression of each gene or for the expression of each gene normalized for CD68 expression as continuous variables, for the evaluation of T1RS signature or TAM marker genes respectively.

Survival analysis on IL1B+ TAMs gene signature. The 6-gene prognostic signature for IL1B+ TAMs, obtained as previously described, was used to stratified patients for survival analysis.

The mean expression of the signature, normalized by CD68 expression, was used to group samples into high and low groups according to the upper and the lower quartile respectively. Cox regression model was fit to compare the high group against the low group, extracting the hazard ratio and its associated p-value.

Association of T1RS and IL1B+ TAMs signatures. Using the TCGAbiolinks R package (v 2.28.3), we downloaded transcriptomic data and clinical data from the aforementioned cohorts. We grouped patients based on the mean expression of the 6-gene IL1B+ TAMs signature normalized by CD68 expression into high, intermediate and low groups according to the upper and the lower quartile of the score distribution. To examine association between IL1B+ TAMs and T1RS signature, we then computed the mean of log2-transformed expression values of T1RS signature genes for each group of patients.

Cell type deconvolution of TCGA PDAC samples. To estimate macrophage proportion in TCGA samples we used CIBERSORTx[58] online tool to deconvolute cell fractions using our annotated scRNA-Seq human PDAC dataset as reference. To build the signature matrix file, we first down-sampled our scRNA-Seq human PDAC dataset, randomly selecting 200 cells for each annotated cell type. We then ran CIBERSORTx to generate cell-type signature matrices and impute the relative cell fractions in each tumor sample, enabling S-mode batch correction.

Quantification and statistical analyses. Results are illustrated as mean ± SD. Graphs show data from at least two independent repeats. Significance was defined as $p < 0.05$. Statistical analysis was conducted either using GraphPad Prism v9.0 (GraphPad Software) or R v3.4.1 (R project). Statistical tests, exact value of n, what n represents are mentioned in the Fig. legends.

Data Availability. Single-cell, Spatial Transcriptomic and bulk RNA-seq data have been deposited at NCBI GEO data repository under the accession number GSE217847. Reviewers can access the full data at the link below (password epklkweqxzqdvqt)

https://www.ncbi.nlm.nih.gov/geo/query/acc.cgi?acc=GSE217847

METHODS REFERENCES

1 Olive, K. P. *et al.* Inhibition of Hedgehog signaling enhances delivery of chemotherapy in a mouse model of pancreatic cancer. *Science* **324**, 1457-1461, doi:10.1126/science.1171362 (2009).

2 Cappello, P. *et al.* Vaccination with ENO1 DNA prolongs survival of genetically engineered mice with pancreatic cancer. *Gastroenterology* **144**, 1098-1106, doi:10.1053/j.gastro.2013.01.020 (2013).

3 Hingorani, S. R. *et al.* Trp53R172H and KrasG12D cooperate to promote chromosomal instability and widely metastatic pancreatic ductal adenocarcinoma in mice. *Cancer Cell* **7**, 469-483, doi:10.1016/j.ccr.2005.04.023 (2005).

4 Corbett, T. H. *et al.* Induction and chemotherapeutic response of two transplantable ductal adenocarcinomas of the pancreas in C57BL/6 mice. *Cancer Res* **44**, 717-726 (1984).

5 Labun, K. *et al.* CHOPCHOP v3: expanding the CRISPR web toolbox beyond genome editing. *Nucleic Acids Res* **47**, W171-W174, doi:10.1093/nar/gkz365 (2019).

6 Pelly, V. S. *et al.* Anti-Inflammatory Drugs Remodel the Tumor Immune Environment to Enhance Immune Checkpoint Blockade Efficacy. *Cancer Discov* **11**, 2602-2619, doi:10.1158/2159-8290.CD-20-1815 (2021).

7 Baker, L. A. & Tuveson, D. A. Generation and Culture of Tumor and Metastatic Organoids from Murine Models of Pancreatic Ductal Adenocarcinoma. *Methods Mol Biol* **1882**, 117-133, doi:10.1007/978-1-4939-8879-2_10 (2019).

8 Milani, M. *et al.* Genome editing for scalable production of alloantigen-free lentiviral vectors for in vivo gene therapy. *EMBO Mol Med* **9**, 1558-1573, doi:10.15252/emmm.201708148 (2017).

9 Zheng, G. X. *et al.* Massively parallel digital transcriptional profiling of single cells. *Nat Commun* **8**, 14049, doi:10.1038/ncomms14049 (2017).

10 Germain, P. L., Lun, A., Garcia Meixide, C., Macnair, W. & Robinson, M. D. Doublet identification in single-cell sequencing data using scDblFinder. *F1000Res* **10**, 979, doi:10.12688/f1000research.73600.2 (2021).

11 Haghverdi, L., Lun, A. T. L., Morgan, M. D. & Marioni, J. C. Batch effects in single-cell RNA-sequencing data are corrected by matching mutual nearest neighbors. *Nat Biotechnol* **36**, 421-427, doi:10.1038/nbt.4091 (2018).

12 Korsunsky, I. *et al.* Fast, sensitive and accurate integration of single-cell data with Harmony. *Nat Methods* **16**, 1289-1296, doi:10.1038/s41592-019-0619-0 (2019).

13 Becht, E. *et al.* Dimensionality reduction for visualizing single-cell data using UMAP. *Nat Biotechnol*, doi:10.1038/nbt.4314 (2018).

14 Gao, R. *et al.* Delineating copy number and clonal substructure in human tumors from single-cell transcriptomes. *Nat Biotechnol* **39**, 599-608, doi:10.1038/s41587-020-00795-2 (2021).

15 Yu, G., Wang, L. G., Han, Y. & He, Q. Y. clusterProfiler: an R package for comparing biological themes among gene clusters. *OMICS* **16**, 284-287, doi:10.1089/omi.2011.0118 (2012).

16 Durinck, S., Spellman, P. T., Birney, E. & Huber, W. Mapping identifiers for the integration of genomic datasets with the R/Bioconductor package biomaRt. *Nat Protoc* **4**, 1184-1191, doi:10.1038/nprot.2009.97 (2009).

17 Setty, M. *et al.* Characterization of cell fate probabilities in single-cell data with Palantir. *Nat Biotechnol* **37**, 451-460, doi:10.1038/s41587-019-0068-4 (2019).

18 Wolf, F. A., Angerer, P. & Theis, F. J. SCANPY: large-scale single-cell gene expression data analysis. *Genome Biol* **19**, 15, doi:10.1186/s13059-017-1382-0 (2018).

19 La Manno, G. *et al.* RNA velocity of single cells. *Nature* **560**, 494-498, doi:10.1038/s41586-018-0414-6 (2018).

20 Bergen, V., Lange, M., Peidli, S., Wolf, F. A. & Theis, F. J. Generalizing RNA velocity to transient cell states through dynamical modeling. *Nat Biotechnol* **38**, 1408-1414, doi:10.1038/s41587-020-0591-3 (2020).

21 Lange, M. *et al.* CellRank for directed single-cell fate mapping. *Nat Methods* **19**, 159-170, doi:10.1038/s41592-021-01346-6 (2022).

22 Reuter, B., Weber, M., Fackeldey, K., Roblitz, S. & Garcia, M. E. Generalized Markov State Modeling Method for Nonequilibrium Biomolecular Dynamics: Exemplified on Amyloid beta Conformational Dynamics Driven by an Oscillating Electric Field. *J Chem Theory Comput* **14**, 3579-3594, doi:10.1021/acs.jctc.8b00079 (2018).

23 Schiebinger, G. *et al.* Optimal-Transport Analysis of Single-Cell Gene Expression Identifies Developmental Trajectories in Reprogramming. *Cell* **176**, 928-943 e922, doi:10.1016/j.cell.2019.01.006 (2019).

24 Liberzon, A. *et al.* The Molecular Signatures Database (MSigDB) hallmark gene set collection. *Cell Syst* **1**, 417-425, doi:10.1016/j.cels.2015.12.004 (2015).

25 Ostuni, R. *et al.* Latent enhancers activated by stimulation in differentiated cells. *Cell* **152**, 157-171, doi:10.1016/j.cell.2012.12.018 (2013).

26 Cilenti, F. *et al.* A PGE2-MEF2A axis enables context-dependent control of inflammatory gene expression. *Immunity*, doi:10.1016/j.immuni.2021.05.016 (2021).

27 Street, K. *et al.* Slingshot: cell lineage and pseudotime inference for single-cell transcriptomics. *BMC Genomics* **19**, 477, doi:10.1186/s12864-018-4772-0 (2018).

28 Browaeys, R., Saelens, W. & Saeys, Y. NicheNet: modeling intercellular communication by linking ligands to target genes. *Nat Methods* **17**, 159-162, doi:10.1038/s41592-019-0667-5 (2020).

29 Peng, J. *et al.* Single-cell RNA-seq highlights intra-tumoral heterogeneity and malignant progression in pancreatic ductal adenocarcinoma. *Cell Res* **29**, 725-738, doi:10.1038/s41422-019-0195-y (2019).

30 Lee, B. *et al.* Single-cell sequencing unveils distinct immune microenvironments with CCR6-CCL20 crosstalk in human chronic pancreatitis. *Gut* **71**, 1831-1842, doi:10.1136/gutjnl-2021-324546 (2022).

31 Burdziak, C. *et al.* Epigenetic plasticity cooperates with cell-cell interactions to direct pancreatic tumorigenesis. *Science* **380**, eadd5327, doi:10.1126/science.add5327 (2023).

32 Sharma, A. *et al.* Onco-fetal Reprogramming of Endothelial Cells Drives Immunosuppressive Macrophages in Hepatocellular Carcinoma. *Cell* **183**, 377-394 e321, doi:10.1016/j.cell.2020.08.040 (2020).

33 Kim, N. *et al.* Single-cell RNA sequencing demonstrates the molecular and cellular reprogramming of metastatic lung adenocarcinoma. *Nat Commun* **11**, 2285, doi:10.1038/s41467-020-16164-1 (2020).

34 Couturier, C. P. *et al.* Single-cell RNA-seq reveals that glioblastoma recapitulates a normal neurodevelopmental hierarchy. *Nat Commun* **11**, 3406, doi:10.1038/s41467-020-17186-5 (2020).

35 Lee, H. O. *et al.* Lineage-dependent gene expression programs influence the immune landscape of colorectal cancer. *Nat Genet* **52**, 594-603, doi:10.1038/s41588-020-0636-z (2020).

36 Azizi, E. *et al.* Single-Cell Map of Diverse Immune Phenotypes in the Breast Tumor Microenvironment. *Cell* **174**, 1293-1308 e1236, doi:10.1016/j.cell.2018.05.060 (2018).

37 Obradovic, A. *et al.* Single-cell protein activity analysis identifies recurrence-associated renal tumor macrophages. *Cell* **184**, 2988-3005 e2916, doi:10.1016/j.cell.2021.04.038 (2021).

38 Stuart, T. *et al.* Comprehensive Integration of Single-Cell Data. *Cell* **177**, 1888-1902 e1821, doi:10.1016/j.cell.2019.05.031 (2019).

39 Lopez, R. *et al.* DestVI identifies continuums of cell types in spatial transcriptomics data. *Nat Biotechnol* **40**, 1360-1369, doi:10.1038/s41587-022-01272-8 (2022).

40 Dries, R. *et al.* Giotto: a toolbox for integrative analysis and visualization of spatial expression data. *Genome Biol* **22**, 78, doi:10.1186/s13059-021-02286-2 (2021).

41 Stirling, D. R. *et al.* CellProfiler 4: improvements in speed, utility and usability. *BMC Bioinformatics* **22**, 433, doi:10.1186/s12859-021-04344-9 (2021).

42 Palla, G. *et al.* Squidpy: a scalable framework for spatial omics analysis. *Nat Methods* **19**, 171-178, doi:10.1038/s41592-021-01358-2 (2022).

43 Guilliams, M. *et al.* Spatial proteogenomics reveals distinct and evolutionarily conserved hepatic macrophage niches. *Cell* **185**, 379-396 e338, doi:10.1016/j.cell.2021.12.018 (2022).

44 Stringer, C., Wang, T., Michaelos, M. & Pachitariu, M. Cellpose: a generalist algorithm for cellular segmentation. *Nat Methods* **18**, 100-106, doi:10.1038/s41592-020-01018-x (2021).

45 Petukhov, V. *et al.* Cell segmentation in imaging-based spatial transcriptomics. *Nat Biotechnol* **40**, 345-354, doi:10.1038/s41587-021-01044-w (2022).
46 Bergenstrahle, J., Larsson, L. & Lundeberg, J. Seamless integration of image and molecular analysis for spatial transcriptomics workflows. *BMC Genomics* **21**, 482, doi:10.1186/s12864-020-06832-3 (2020).
47 Carpenter, E. S. *et al.* Analysis of donor pancreata defines the transcriptomic signature and microenvironment of early pre-neoplastic pancreatic lesions. *bioRxiv*, doi:10.1101/2023.01.13.523300 (2023).
48 Ritchie, M. E. *et al.* limma powers differential expression analyses for RNA-sequencing and microarray studies. *Nucleic Acids Res* **43**, e47, doi:10.1093/nar/gkv007 (2015).
49 Picelli, S. *et al.* Full-length RNA-seq from single cells using Smart-seq2. *Nat Protoc* **9**, 171-181, doi:10.1038/nprot.2014.006 (2014).
50 Dobin, A. *et al.* STAR: ultrafast universal RNA-seq aligner. *Bioinformatics* **29**, 15-21, doi:10.1093/bioinformatics/bts635 (2013).
51 Liao, Y., Smyth, G. K. & Shi, W. The R package Rsubread is easier, faster, cheaper and better for alignment and quantification of RNA sequencing reads. *Nucleic Acids Res* **47**, e47, doi:10.1093/nar/gkz114 (2019).
52 Pruitt, K. D., Tatusova, T. & Maglott, D. R. NCBI reference sequences (RefSeq): a curated non-redundant sequence database of genomes, transcripts and proteins. *Nucleic Acids Res* **35**, D61-65, doi:10.1093/nar/gkl842 (2007).
53 Robinson, M. D., McCarthy, D. J. & Smyth, G. K. edgeR: a Bioconductor package for differential expression analysis of digital gene expression data. *Bioinformatics* **26**, 139-140, doi:10.1093/bioinformatics/btp616 (2010).
54 Robinson, M. D. & Oshlack, A. A scaling normalization method for differential expression analysis of RNA-seq data. *Genome Biol* **11**, R25, doi:10.1186/gb-2010-11-3-r25 (2010).
55 Alonso-Curbelo, D. *et al.* A gene-environment-induced epigenetic program initiates tumorigenesis. *Nature* **590**, 642-648, doi:10.1038/s41586-020-03147-x (2021).
56 Montaldo, E. *et al.* Cellular and transcriptional dynamics of human neutrophils at steady state and upon stress. *Nat Immunol* **23**, 1470-1483, doi:10.1038/s41590-022-01311-1 (2022).
57 Colaprico, A. *et al.* TCGAbiolinks: an R/Bioconductor package for integrative analysis of TCGA data. *Nucleic Acids Res* **44**, e71, doi:10.1093/nar/gkv1507 (2016).
58 Newman, A. M. *et al.* Determining cell type abundance and expression from bulk tissues with digital cytometry. *Nat Biotechnol* **37**, 773-782, doi:10.1038/s41587-019-0114-2 (2019).